

Role of fault gouge dilatancy on aseismic deformation transients

Yajing Liu¹ and Allan M. Rubin²

Received 2 March 2010; revised 12 July 2010; accepted 21 July 2010; published 16 October 2010.

[1] In the vicinity of episodic aseismic transients in several subduction zones, the presence of interstitial fluids and near-lithostatic pore pressure has been proposed to interpret seismic observations of high P to S wave speed ratio and high Poisson's ratio. Under such conditions, fault stabilization by dilatancy-induced suction during increased shear strain rates becomes very efficient. We analyze the frictional and hydraulic conditions for spontaneous transients on a fluid-infiltrated fault including dilatancy and pore compaction in the framework of rate and state friction with a "membrane diffusion" approximation. In both a simplified spectral model and a 2-D Cascadia-like subduction fault model, the fault response is mainly controlled by three nondimensional parameters: (1) W/h^* , the along-dip width of the high pore pressure, velocity-weakening fault relative to a characteristic nucleation size, (2) a drainage parameter U , the relative time scales for fluid diffusion and friction evolution, and (3) a dilatancy parameter E , the relative contributions to stress drop from dilatancy and friction evolution. The incorporation of dilatancy enables aseismic transients at much larger values of W/h^* than is possible under conditions of constant pore pressure. An analytic estimate of the maximum slip velocity as a function of W/h^* , E , and U is derived and agrees reasonably well with the simulation results. The dependence of the properties of modeled transients on the drainage parameter U is similar to that on the dilatancy parameter E . For U (E) less than 1, maximum velocity decreases, while recurrence period remains relatively constant. For U (E) greater than 1, maximum velocity approaches the steady state velocity, and recurrence period approaches the period at neutral stability. In the subduction fault model using gabbro gouge friction properties, the slip per episode and the recurrence period increase with W/h^* , generally following the trend defined without dilatancy. The maximum velocity with dilatancy can be several orders of magnitude smaller than that without, in particular for larger values of E and values of W/h^* near the no-dilatancy stability limit.

Citation: Liu, Y., and A. M. Rubin (2010), Role of fault gouge dilatancy on aseismic deformation transients, *J. Geophys. Res.*, 115, B10414, doi:10.1029/2010JB007522.

1. Introduction

[2] Recently observed episodic aseismic deformation transients (also called slow slip events, SSEs), sometimes accompanied by low-frequency tremors, at 30–40 km in subduction zones [e.g., Hirose *et al.*, 1999; Dragert *et al.*, 2001; Lowry *et al.*, 2001], have been proposed to occur along subduction plate interfaces under highly elevated pore pressure. There are several lines of evidence supporting the presence of near-lithostatic fluid pressure in the source areas of transients and nonvolcanic tremors. First, metamorphic dehydration reactions are encountered as temperature and pressure increase in the oceanic crust of subduction zones where short-period transients have been observed (e.g., Cascadia, southwest Japan and south Mexico) [Peacock

et al., 2002; Hacker *et al.*, 2003; Wada *et al.*, 2008]. Second, seismological observations imply high P to S wave speed ratio and hence high Poisson's ratio in the vicinity of the subduction plate interfaces in SW Japan and northern Cascadia, coincident with the depth ranges of transients [Kodaira *et al.*, 2004; Shelly *et al.*, 2006; Audet *et al.*, 2009]. In particular, high Poisson's ratio of ≥ 0.4 is estimated at ~ 20 –40 km depth in the northern Cascadia subduction zone [Audet *et al.*, 2009], strongly indicating near-lithostatic fluid pressure [Christensen, 1984]. Third, extremely small stress perturbations of order 0.01 MPa due to teleseismic surface waves or tidal stressing can sometimes trigger nonvolcanic tremors in transients source areas [Miyazawa and Mori, 2006; Rubinstein *et al.*, 2007; Gomberg *et al.*, 2008; Peng *et al.*, 2008b], which suggests the background effective normal stress ($\bar{\sigma} = \sigma - p$, difference between normal stress and pore pressure, compression positive) is possibly very low for such triggering to be effective. In addition, taking the inferred maximum slip velocity (V_{\max}) of 10^{-8} to 10^{-7} m s⁻¹, and slip propagation speed (v_r) of order of km d⁻¹ of typical transients, numerical studies have estimated $\bar{\sigma}$ of

¹Department of Geology and Geophysics, Woods Hole Oceanographic Institution, Woods, Hole, Massachusetts, USA.

²Department of Geosciences, Princeton, University, Princeton, New Jersey, USA.

only a few MPa, in order to satisfy an analytical relation between V_{\max} , v_r and shear stress drop derived for an expanding nucleation zone subject to rate and state friction [Shibazaki and Shimamoto, 2007; Ampuero and Rubin, 2008; Rubin, 2008].

[3] Numerical simulations in the framework of rate- and state-dependent friction have demonstrated that short-period aseismic deformation transients can emerge spontaneously when interstitial fluids are present and pore pressure is near-lithostatic around the friction stability transition, for certain friction parameter variations along a thrust fault loaded by a constant plate convergence rate V_{pl} [Liu and Rice, 2005a, 2007; Shibazaki and Shimamoto, 2007; Rubin, 2008]. Applying temperature (and hence depth) variable rate and state friction parameters of granite [Blanpied *et al.*, 1998] and gabbro gouges [He *et al.*, 2007] to a 2-D subduction earthquake model with the “aging” evolution law, Liu and Rice [2007, 2009] found that episodic transients occur when the near-lithostatic pore pressure velocity-weakening fault width is too large for steady sliding but too small for dynamic instability. Such numerical simulations can produce spontaneous transients with aspects that share similar characteristics with those inferred from geodetic observations. Liu and Rice [2007] showed that the modeled recurrence period increases with the level of effective normal stress. For a Cascadia-like subduction fault model using the wet granite gouge friction data, a 1–2 year period is achieved at $\bar{\sigma} \sim 2\text{--}3$ MPa when most of the updip seismogenic zone is completely locked. The accumulated slip per episode is about 1–2 cm on the subduction interface. The above numerical studies of the mechanisms of SSEs have assumed the effective normal stress on the fault to be time invariant. However, fluid pressure variation along the fault interface may also influence the occurrence and migration of slow slip events and tremors. In particular, the proposed high fluid pressure, or equivalently low effective normal stress, is precisely the condition for which Segall and Rice [1995] suggested that fault stabilization by induced suction from dilatancy during increased shear rates becomes very efficient.

[4] Porosity in granular materials evolves as shear begins. After a certain amount of deformation, a critical state is reached where porosity and pore pressure remain constant [Schofield and Wroth, 1968]. For fluid-saturated materials, if dilatancy occurs more rapidly than pore fluid can flow into the newly created void space (e.g., due to uplift in sliding over contact asperities), the local pore pressure is reduced and the effective normal stress is increased (compression positive). This dilatancy-strengthening process has been suggested to play a role in inhibiting rapid deformations of landslides [e.g., Iverson *et al.* 2000], glacier basal sediments [Clarke, 1987; Iverson *et al.*, 1998] and fault gouges [Marone *et al.*, 1990; Lockner and Byerlee, 1994]. Marone *et al.* [1990] investigated the frictional properties on a simulated fault gouge (quartz sand) under saturated drained (constant pore pressure) conditions in response to velocity steps. In their experiments, step increases in sliding velocity were accompanied by porosity increases (dilation), while step drops were accompanied by porosity decreases (compaction). Following such velocity steps, porosity evolved toward a new steady state over a distance comparable to the evolution distance of friction, suggesting a

connection between the two processes. Lockner and Byerlee [1994] also conducted frictional experiments using Ottawa sand as the gouge material under both drained and undrained (constant pore fluid mass). They found the frictional resistance increased as a result of the pore suction under the undrained condition.

[5] Shear-induced pore pressure suction and consequent frictional strengthening have important implications for the nucleation of earthquake slip on natural faults. Sleep and Blanpied [1992] presented quantitative models of earthquake cycles, in which pore pressure increases due to pore compaction during the interseismic period until a Coulomb slip condition is satisfied, followed by a rapid slip event (model earthquake) with pore pressure dropping to the initial level due to dilatancy. Sleep [1995] improved the model by including the explicit instability condition for combined slip weakening, frictional dilatancy and shear heating induced thermal pressurization [Sibson, 1973; Lachenbruch, 1980; Mase and Smith, 1987]. Segall and Rice [1995] incorporated both processes of dilatancy and pore compaction into the rate and state friction model, to understand the conditions for unstable slip on saturated fault gouge. They assumed that the actively slipping interface is bordered by a less permeable layer, within which pore pressure varies linearly from the level on the interface to the ambient level in the surrounding rock mass. This is called a “membrane diffusion” (or “lumped reservoir”) approximation, previously used by Rudnicki and Chen [1988] in an analysis of laboratory experiments of dilatancy strengthening. Linearized perturbation analysis of a single-degree-of-freedom spring-slider model at steady sliding shows that slip is always stable when the effective normal stress is smaller than a threshold which is determined by the fault gouge frictional and hydraulic properties [Segall and Rice, 1995]. The higher the pore pressure on the sliding interface, the more important dilatancy is in stabilizing slip. Taylor and Rice [1998] first included dilatancy in a 2-D subduction fault model with rate and state friction to study its effects on earthquake rupture in the radiation damping approximation [Rice, 1993]. They found that quasi-dynamic seismic rupture slows down or even stops where effective normal stress is lower than that in the seismogenic zone; without dilatancy seismic slip of several meters would occur where the fault breaches the surface. Dilatancy was also incorporated in a 3-D continuum model governed by rate and state friction to study the effects of spatial variations in pore pressure on spatiotemporal slip evolution along a hydraulically isolated fault [Hillers and Miller, 2007].

[6] Building on the work by Taylor and Rice [1998], Liu and Rice [2005b] and Segall and Rubin [2007], in this paper we analyze the conditions for spontaneous short-period aseismic transients on a fluid-infiltrated subduction fault governed by the rate and state friction (“aging” evolution) law, including dilatancy and pore compaction, with the “membrane diffusion” approximation. Numerical simulations in a simplified spectral model and a Cascadia-like 2-D subduction fault model show that the incorporation of dilatancy enables periodic or quasiperiodic aseismic transients over a much broader range of fault width than is possible in the absence of dilatancy. We analyze the dependence of key SSE characteristics, such as the maximum slip velocity, recurrence period and cumulative slip

Table 1. Typical Model Notations, Definitions, and Equation Number Where They Are Defined or First Appear^a

Notation	Definition	Value (Unit)	Equation
a, b	Friction parameters		(1)
c	Hydraulic diffusivity		(7)
d_c	Characteristic slip distance		(1)
d_p	Low permeability zone thickness		
f	Friction coefficient		(1)
f_0	Nominal friction	0.6	
f_{ss}	Steady state friction		
h	Model grid size		
h^*	Characteristic nucleation size (1)		(3)
k	Effective stiffness		
k_{cr}, k_{cr}^{dilat}	Critical stiffness (drained, with dilatancy)		(22)
m	Fluid mass per unit rock volume		(4)
p	Pore pressure on fault		(5)
p_0	Ambient pore pressure		(8)
q_m	Fluid mass flux per unit area		(4)
t	Time in numerical simulations		
t_p	Characteristic diffusion time		(8)
v_r	Slip propagation speed		(20)
α	Coefficient in h^* definition		(3)
β	Fluid and pore space bulk compressibility		(6)
β_f	Isothermal fluid compressibility		
β_ϕ	Isothermal elastic pore compressibility		
γ	Prefactor in $v_r - V_{max}$ relation		
γ_f	Isobaric fluid expansion coefficient		(6)
γ_ϕ	Isobaric pore expansion coefficient		(6)
δ	Slip on the fault		
ϵ	Dilatancy coefficient		(9)
ζ	Distance normal to fault		(4)
η	Fluid viscosity		(5)
θ	State variable		(1)
θ_i	State variable prior to the arrival of crack tip		(12)
κ	Fault-normal permeability		(5)
μ	Shear modulus	30 (GPa)	
μ'	Effective shear modulus	40 (GPa)	(3)
ν	Poisson's ratio	0.25	
ξ	Distance along fault		
ρ	Fluid density		(5)
$\bar{\sigma}$	Effective normal stress		(1)
$\bar{\sigma}_0$	Initial effective normal stress		
τ	Shear stress		(1)
ϕ	Fault gouge porosity		(6), (9)
ϕ_{pl}	Plastic porosity		(6)
ϕ_0	Reference porosity		(9)
E	Dilatancy parameter		(14)
E_p	Dilatancy efficiency parameter in Segall <i>et al.</i> [2010]		
G	Mechanical energy release		
G^c	Total fracture energy		
$G_{\Delta p}^c$	Fracture energy dominated by pore suction		(B1)
L_b	Characteristic nucleation size (2)		
T	Fluid temperature on fault interface		(6)
T_{cyc}	Modeled transients recurrence period		
T_{ns}	Neutral stability period		
U	Drainage parameter		(11)
V	Slip velocity		
V_0	Reference slip velocity		(1)
V_{dyn}	Dynamic slip velocity		(16)
V_{max}	Max. velocity on the fault		
V_{pl}	Plate convergence rate	37 (mm yr ⁻¹)	
V_{ss}	Steady state velocity		(17)
W	Velocity-weakening fault under high pore pressure		(17) (18)
W'	Fault width where rate and state friction is applied		
W/h_{dilat}^*	W/h^* with dilatancy		(22)

Table 1. (continued)

Notation	Definition	Value (Unit)	Equation
Λ	Thermal pressurization parameter		(6)
Δp_{max}	Max. pore suction		(A8)
Δp^{p-r}	Max. pore pressure drop (undrained)		(12)
$\Delta \tau^{p-r}$	Peak-to-residual shear stress drop		(13)
$\Delta \tau^{f-r}$	Total shear stress drop		(15)

^aParameter values are also given if they are constant in all simulation cases.

during each episode, on three nondimensional parameters W/h^* , E and U . Here W/h^* is the ratio of near-lithostatic pore pressure velocity-weakening fault width to a characteristic nucleation size; drainage parameter U describes the relative time scales of pore pressure diffusion and friction evolution; and dilatancy parameter E describes the relative contributions to shear stress drop from pore dilation and friction evolution in the slow slipping process. Definitions and physical interpretations of the three parameters are discussed in detail in section 2. Slip velocity and pore pressure evolution processes are analyzed for modeled slow slip events with representative parameters, and shown to agree reasonably well with analytical or semi-analytical estimates. This paper is structured as follows. Section 2 introduces the governing constitutive equations including rate and state friction, pore fluid diffusion and porosity evolution. Section 3 describes dilatancy effects on aseismic deformation transients in a simplified spectral model and a 2-D subduction fault model. Discussion and conclusions are in sections 4 and 5.

2. Constitutive Models

2.1. Rate and State Friction

[7] We use a single-state-variable form of the rate and state-dependent friction law, in which the frictional resistance τ is a function of the sliding velocity V and the state variable θ ; under steady state conditions θ can be interpreted as the average asperity contact time [Dieterich, 1979; Ruina, 1983]. In particular,

$$\tau = \bar{\sigma}f = (\sigma - p) \left[f_0 + a \ln \left(\frac{V}{V_0} \right) + b \ln \left(\frac{V_0 \theta}{d_c} \right) \right], \quad (1)$$

where effective normal stress $\bar{\sigma}$ is the difference between the normal stress σ applied on the fault and pore pressure p ; a and b are rate and state friction parameters, V_0 is a reference velocity, taken to be 10^{-6} m s⁻¹ in the following numerical calculations, and d_c is the characteristic slip distance over which state evolves after a velocity step; f_0 is a nominal friction when $V = V_0$ at steady state (see Table 1). In this study, we use the ‘‘aging’’ state evolution law, which permits friction to evolve on stationary contacts, as observed in lab experiments [Beeler *et al.*, 1994],

$$\frac{d\theta}{dt} = 1 - \frac{V\theta}{d_c}. \quad (2)$$

The relatively less fine numerical resolution requirement by using the ‘‘aging’’ law, compared to the other commonly used version of state evolution ‘‘slip’’ law, also allows us to

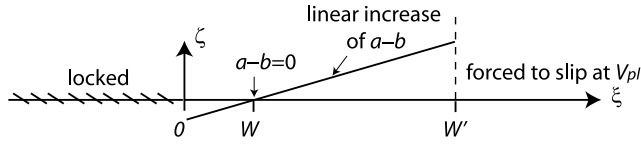


Figure 1. Geometry and $a-b$ distribution for the 1-D spatially periodic fault model. The fault is locked at $-8W < \xi < 0$, velocity weakening at $0 \leq \xi \leq W$, velocity strengthening at $W < \xi \leq W'$, and loaded by a constant V_{pl} at $W' < \xi < W' + 8W$. $W'/W = 4$ for most simulation cases if not otherwise stated; $a-b$ linearly increases from -0.004 to 0.012 , and $b = 0.034$ is uniform between $0 \leq \xi \leq W$.

explore extensively the large parameter space defined by W/h^* , E and U . Study of the dilatancy effect on slow slip events using “slip” law is presented by *Segall et al.* [2010]. Both evolution laws result in the same steady state friction $f_{ss} = f_0 + (a - b)\ln(V/V_0)$, when $\theta = \theta_{ss} = d_c/V$.

[8] The constitutive parameters a and $a-b$ are interpreted as the instantaneous change in f and change in f_{ss} , respectively, in response to a velocity step: $a = V(\partial f/\partial V)_{inst}$ and $a - b = V(df_{ss}/dV)$. For $a - b > 0$, the sliding surface is steady state velocity strengthening and slip is stable. For $a - b < 0$, the interface is steady state velocity weakening and unstable slip is possible when, for a single-degree-of-freedom spring-slider system subject to small perturbations from steady sliding, the spring stiffness is less than the drained critical stiffness $k_{cr} = \bar{\sigma}(b - a)/d_c$. A critical nucleation size h^* is defined by equating k_{cr} to the effective stiffness $k = \alpha\mu'/h$ at the center of a crack of width h ,

$$h^* = \alpha \frac{\mu' d_c}{\bar{\sigma}(b - a)}. \quad (3)$$

Here α is a model-dependent constant of order unity; $\alpha = 2/\pi$ when using the cellular basis set for slip (shear stress τ is calculated as if slip were locally uniform on each cell) on a crack that is not too close to the surface. Effective shear modulus $\mu' = \mu$ for anti-plane strain and $\mu' = \mu/(1 - \nu)$ for plane strain deformation, where ν is Poisson’s ratio; we use $\mu = 30$ GPa and $\nu = 0.25$ in this paper. For a fault segment with nonuniform $b-a$ distribution, an average value $\langle b - a \rangle$ is used in equation (3).

2.2. Governing Equations for Fluid

[9] We follow *Segall and Rice* [1995] and *Taylor and Rice* [1998] in the treatment of fluid diffusion and pore compaction associated with friction evolution. For the planar fault model considered here, we assume that fluid (water) flux is limited to the direction ζ perpendicular to the fault and that there is no flux in the direction ξ parallel to the fault (Figure 1). The reason for neglecting the fault-parallel flux will be explained after equation (7). The conservation of fluid mass implies that

$$\frac{\partial q_m}{\partial \zeta} + \frac{\partial m}{\partial t} = 0, \quad (4)$$

where m is the fluid mass per unit volume of rock and q_m is the fluid mass flux per unit area. Fluid flux is related to the pore pressure gradient via Darcy’s law

$$q_m = -\frac{\rho\kappa}{\eta} \frac{\partial p}{\partial \zeta}, \quad (5)$$

where ρ is the fluid density, κ is the permeability for diffusion normal to the fault, and η is the fluid viscosity. The rate of fluid mass change can be written as

$$\begin{aligned} \frac{\partial m}{\partial t} &= \phi \frac{\partial \rho}{\partial t} + \rho \frac{\partial \phi}{\partial t} \\ &= \rho \phi \left(\beta_f \frac{\partial p}{\partial t} - \gamma_f \frac{\partial T}{\partial t} \right) + \rho \phi \left(\beta_\phi \frac{\partial p}{\partial t} + \gamma_\phi \frac{\partial T}{\partial t} \right) + \rho \frac{\partial \phi_{pl}}{\partial t} \\ &= \rho \beta \left(\frac{\partial p}{\partial t} - \Lambda \frac{\partial T}{\partial t} + \frac{1}{\beta} \frac{\partial \phi_{pl}}{\partial t} \right), \end{aligned} \quad (6)$$

where ϕ is porosity and T is temperature; $\beta_f \equiv (1/\rho)(\partial \rho/\partial p)_T$ and $\beta_\phi \equiv (1/\phi)(\partial \phi/\partial p)_T$ are isothermal fluid compressibility and elastic pore compressibility, respectively; $\gamma_f \equiv - (1/\rho)(\partial \rho/\partial T)_p$ and $\gamma_\phi \equiv (1/\phi)(\partial \phi/\partial T)_p$ are fluid expansion coefficient and pore expansion coefficient, respectively, at constant pressure. The bulk (fluid and pore space) compressibility parameter is defined as $\beta = \phi(\beta_f + \beta_\phi)$ and thermal pressurization parameter $\Lambda = (\gamma_f - \gamma_\phi)/(\beta_f + \beta_\phi)$. The change in porosity is written as the sum of an elastic component that is related to the changes in p and T via β_ϕ and γ_ϕ , respectively, and a plastic component ϕ_{pl} that later will be assumed to be related to the state variable θ . Here we neglect the full poroelastic coupling and assume the dependence of the elastic porosity component on pore pressure is at conditions of fixed fault-normal stress and fixed fault-parallel strain.

[10] Substituting (5) and (6) into (4), we get the pore pressure diffusion equation with source terms due to the plastic porosity change and temperature change

$$c \frac{\partial^2 p}{\partial \zeta^2} - \frac{\partial p}{\partial t} = \frac{1}{\beta} \frac{\partial \phi_{pl}}{\partial t} - \Lambda \frac{\partial T}{\partial t}, \quad (7)$$

where the hydraulic diffusivity $c = \kappa/(\eta\beta)$ is defined assuming spatially uniform ρ , η and κ . For a hydraulic diffusivity of $10^{-8} \text{ m}^2 \text{ s}^{-1}$ (taking $\kappa = 10^{-20} \text{ m}^2$, $\eta = 10^{-3} \text{ Pa s}$, and $\beta = 5 \times 10^{-4} \text{ MPa}^{-1}$ as shown later in this section), a perturbation in p diffuses along the dip direction on the order of a few meters in a representative 1–2 year slow slip cycle. This indicates extremely small gradients along the fault, compared to the slow slip events of characteristic dimension of tens of kilometers. For the same reason, we neglect heat conduction along the fault, as well as heat convection in the pore fluid phase. Thus, temperature T changes due to heat conduction across the fault and heat generation during shear, which is proportional to the product of shear stress and sliding velocity. Both properties are small in the context of slow slip events; $\tau \sim 1$ MPa for $f_0 = 0.6$ and $\bar{\sigma} \sim 1$ –2 MPa and $V \sim 10^{-7}$ to 10^{-8} m s^{-1} . Indeed, in the absence of dilatancy effects, *Segall and Rice* [2006], *Schmitt et al.* [2007] and *Schmitt and Segall* [2008] found that thermal weakening becomes a dominating mechanism only when the sliding velocity is higher than $\sim 10^{-4}$ to 10^{-2} m s^{-1} , using permeabilities measured for active continental crust faults. Thus, the

temperature variation term $\partial T/\partial t$ is neglected in the following analysis of slow slip events.

[11] For the flux normal to the fault, we make the “membrane diffusion” approximation so that equation (7) can be written as

$$\frac{\partial p}{\partial t} = -\frac{p-p_0}{t_p} - \frac{1}{\beta} \frac{\partial \phi_{pl}}{\partial t}. \quad (8)$$

As in the work by *Segall and Rice* [1995], this approximation applies when the fault is bordered by a low permeability zone of thickness d_p surrounded by rock mass of constant ambient pore pressure p_0 , and slip time is long compared to the diffusion time across that layer. Here $t_p = \eta\beta d_p^2/\kappa$ is a characteristic time for p to reequilibrate with p_0 .

[12] We model the dilatancy term following the analysis by *Sleep* [1995] and *Segall and Rice* [1995], which builds on observations from fault gouge friction experiments at room temperature [*Marone et al.*, 1990]. The plastic component of porosity is assumed to evolve with the state variable θ as

$$\phi_{pl} = \phi_0 - \epsilon \ln\left(\frac{V_0\theta}{d_c}\right), \quad (9)$$

where ϕ_0 is a reference porosity and ϵ is a dimensionless dilatancy coefficient. In lab frictional sliding experiments on simulated fault gouges, $\epsilon = \Delta\phi/\Delta\ln(V)$ measures porosity change associated with shear velocity steps. Equation (8) then becomes

$$\frac{\partial p}{\partial t} = -\frac{p-p_0}{t_p} + \frac{\epsilon}{\beta} \frac{1}{\theta} \frac{d\theta}{dt}. \quad (10)$$

By comparing the *Marone et al.* [1990] laboratory data to their simulations, *Segall and Rice* [1995] estimated the dilatancy coefficient ϵ to be 1.7×10^{-4} for quartz sand under drained conditions. *Samuelson et al.* [2009] reported lab measurements of dilatancy coefficient ranging from 4.7×10^{-5} to 3.0×10^{-4} during velocity-stepping friction experiments conducted on fine-grained quartz fault gouge (mean grain size 127 μm) at effective normal stress of 0.8 to 20 MPa. More recent dilatancy coefficient measurements from Westerly granite and clay-rich ODP gouge are also within the range of 10^{-5} to 10^{-4} , and show a relatively neutral to slightly negative trend with increasing normal stress (J. Samuelson, personal communication, 2010). Bulk compressibility β [= $\phi(\beta_f + \beta_\phi)$] can be estimated following the choices of *Segall and Rice* [1995]. Take water compressibility $\beta_f \sim 5 \times 10^{-4} \text{ MPa}^{-1}$, elastic pore compressibility $\beta_\phi \sim 10^{-2} \text{ MPa}^{-1}$ for crystalline rocks that are more representative of fault gouge at seismogenic depths, and a porosity $\phi = 0.05$ which is at the lower end of the observed range for sufficiently sheared Ottawa sand gouge in the lab [*Marone et al.*, 1990], the bulk compressibility is roughly $5 \times 10^{-4} \text{ MPa}^{-1}$. We note that ϵ and β enter equation (10) only through the ratio ϵ/β , which has the unit of pressure. Therefore, in the following calculations, instead of choosing individual values for ϵ and β , we only specify ϵ/β , which is in the vicinity of 0.34 MPa based on the above estimates.

[13] The rate and state friction law (equations (1) and (2)) and pore pressure evolution (equation (10)) are implemented together with the quasi-static elastic relation between shear stress and slip distributions on the fault, to solve for the evolution of slip velocity, shear stress and pore pressure on the modeled fault in earthquake cycles including slow slip events. A radiation damping term that is correct in dynamic instantaneous response and in producing quasi-static long-term response is introduced following *Rice* [1993] and *Lapusta et al.* [2000].

2.3. Nondimensional Parameters U and E

[14] Evident from equation (10), two competing factors control the rate of pore pressure change. The first factor is the rate at which p communicates with p_0 at the characteristic diffusion time scale t_p . The second is the rate at which p changes due to the opening or closing of pore spaces as the state variable θ evolves at time scale d_c/V . To compare these competing factors, we need to define a velocity scale for V . An obvious choice is the driving plate velocity V_{pl} ($\sim 40 \text{ mm yr}^{-1}$ for northern Cascadia subduction zone). But, because in the model set up in section 3 the SSEs region is adjacent to a locked or nearly locked zone, its average velocity V_{ss} (or its actual steady state velocity, for a simulation with steady sliding) is only a modest fraction of V_{pl} . The degree of drainage of the fault near the transition from steady to oscillatory sliding is thus characterized by a nondimensional drainage parameter

$$U \equiv t_p/(d_c/V_{ss}). \quad (11)$$

When $U \ll 1$, the fault gouge is nearly drained near this transition, and there is no change in pore pressure. Even when $U \ll 1$, the fault will still behave as undrained at slip velocities V sufficiently large that $t_p/(d_c/V) \gg 1$. When $U \gg 1$, the gouge is nearly undrained, and there is no change in fluid mass. On a completely drained fault p instantaneously re-equilibrates with p_0 ; solutions to the coupled equations are essentially the same as those to the system without dilatancy.

[15] As with elastodynamic ruptures on a rate-and-state fault, in response to the passage of the propagating front of a quasi-statically expanding nucleation zone the fault undergoes a near-instantaneous velocity increase [*Rubin and Ampuero*, 2005]. For an increase from V_1 to V_2 under a time-invariant effective normal stress $\bar{\sigma} = \bar{\sigma}_0$, after slip is far enough to reach a new steady state the peak-to-residual stress drop is $\Delta\tau^{p-r} = \bar{\sigma}_0 \Delta f^{p-r} = b\bar{\sigma}_0 \ln(V_2\theta_i/d_c)$, where θ_i is the value of state θ prior to the arrival of the crack tip. The total stress drop is $\Delta\tau^{i-r} = \bar{\sigma}_0 \Delta f^{i-r} \approx (b-a)\bar{\sigma}_0 \ln(V_2\theta_i/d_c)$, if sliding is at steady state before the velocity jump (i.e., $V_1 \approx d_c/\theta_i$). Including the change in pore pressure and assuming that $\bar{\sigma}$ and friction f reach peak values at the same position on the fault, we can write the peak-to-residual stress drop as $\Delta f^{p-r} \approx \bar{\sigma}_0 \Delta f^{p-r} - f_0 \Delta f^{p-r}$ and the total stress drop as $\Delta\tau^{i-r} \approx \bar{\sigma}_0 \Delta f^{i-r} - f_0 \Delta p^{i-r}$. As shown in Appendix A, for a hypothetical velocity jump from an initial state θ_i to a constant speed V_2 associated with an expanding nucleation zone on a fully undrained fault, the maximum pore suction during the state evolution process $\Delta p_{\text{max}} = -(\epsilon/\beta) \ln(V_2\theta_i/d_c)$ is reached at $t \rightarrow \infty$. This provides an upper bound to the peak-to-

residual pore pressure drop on a fault that is essentially undrained on the short time scales associated with the passage of the slipping front but drained well behind the front:

$$\Delta p^{p-r} \approx (\epsilon/\beta) \ln(V_2 \theta_i / d_c), \quad (12)$$

which results in the peak-to-residual stress drop

$$\Delta \tau^{p-r} \approx b \bar{\sigma}_0 (1 - E) \ln(V_2 \theta_i / d_c). \quad (13)$$

Here, the nondimensional dilatancy parameter

$$E \equiv f_0 (\epsilon/\beta) / (b \bar{\sigma}_0) \quad (14)$$

measures the relative contributions to shear stress drop from pore pressure suction and friction evolution. Equation (13) can also be derived from the expression for stress drop in equation (A11), by taking slip $\delta = 0$. Assuming the fault is undrained everywhere, the total stress drop becomes

$$\Delta \tau^{i-r} \approx b \bar{\sigma}_0 (1 - a/b - E) \ln(V_2 \theta_i / d_c). \quad (15)$$

Before performing numerical calculations, some aspects of the nucleation process with dilatancy can be predicted based on the above equations. When $E \ll 1 - a/b$, pore pressure changes are irrelevant because the stress drops are dominated by the friction evolution term, even under completely undrained condition. When $E \ll 1 - a/b$, there is some slip speed at which the fault becomes undrained and (from equation (15)) the stress “drop” becomes stress increase, providing an upper bound to the slip speed. Near-lithostatic pore pressure in the slow slip source region, as has been inferred from some observations, would help to promote this. For example, if we take representative values $f_0 = 0.6$, $\epsilon = 1.7 \times 10^{-4}$, $\beta = 5 \times 10^{-4} \text{ MPa}^{-1}$, $b = 0.006$ as in the work by *Segall and Rice* [1995], $\bar{\sigma}_0 < 33 \text{ MPa}$ will result in $E > 1$. Given $E \ll 1 - a/b$, slow slip events could conceivably arise for any value of U such that

$$U = \frac{V_{ss} t_p}{d_c} \lesssim 1 \lesssim \frac{V_{dyn} t_p}{d_c}, \quad (16)$$

where V_{dyn} is a representative dynamic slip speed. Satisfying the first inequality would allow the slip to accelerate episodically, while satisfying the second prevents it from reaching dynamic speeds. Because V_{dyn} is many orders of magnitude larger than V_{ss} , this would allow slow slip events to occur for orders of magnitude variation in t_p . This stability boundary $E = 1 - a/b$ was also derived by *Segall and Rice* [1995] in a linearized stability analysis for the “membrane diffusion” model with a spring-slider system, and tested in a continuum fault model by *Segall et al.* [2010].

3. Aseismic Deformation Transients

3.1. Simplified Model

[16] To investigate the effects of dilatancy on aseismic deformation transients, we first study the contributions of various parameters in a simplified model fault that is locked for $\xi < 0$ and forced to slip at a constant rate V_{pl} for $\xi > W'$, as shown in Figure 1. Rate and state friction is applied on $0 \leq \xi \leq W'$, where slip is velocity weakening ($a - b < 0$)

on $0 \leq \xi \leq W$ and velocity strengthening ($a - b > 0$) on $W < \xi \leq W'$. Specifically, $a - b$ linearly increases from -0.004 to 0.012 , $b = 0.034$, $d_c = 40 \mu\text{m}$ and $\bar{\sigma}_0$ (varies from case to case) are uniform between $0 \leq \xi \leq W'$. The entire domain, including the “locked,” “forced” and the rate and state frictional sliding segments, is repeated along the ξ direction, so that a spectral method can be applied to solve the coupled equations. A spectral method without spatial replication has been proposed by *Cochard and Rice* [1997] that requires only twice the domain size where the constitutive law between stress and slip is imposed.

[17] Several width ratios shown in Figure 1 are of different extent of relevance to the simulation results. First, the fault widths of the “locked” and “forced” parts have very minor effects, as verified numerically, when they are much larger than W . We use $8W$ for both segments in the spatially periodic model. Second, the ratio W'/W continues to affect the results even when it gets very large. *Rubin* [2008] showed that for infinitely locked and forced regions and $W'/W \gg 1$, the steady slip speed at the center of W is

$$V_{ss} \approx \frac{\sqrt{2}}{\pi} \left(\frac{W}{W'} \right)^{1/2} V_{pl}, \quad (17)$$

and recurrence period varies inversely with V_{ss} [*Rubin*, 2008, equation (22)]. For $W'/W = 4$ in this study, $V_{ss} \approx 0.23 V_{pl}$ at $\xi = W/2$ is used in the definition of U (equation (11)). Among the numerically calculated physical properties, W'/W has relatively small effects on the sliding pattern (i.e., stable, periodic, or unstable) and the maximum velocity during aseismic slip events.

[18] Finally, we learned from 2-D subduction fault simulations [*Liu and Rice*, 2007] that the ratio between W and the critical nucleation size, namely

$$\frac{W}{h^*} = \frac{\pi W \langle b - a \rangle \bar{\sigma}_0}{2 \mu' d_c}, \quad (18)$$

also affects the fault response. Without dilatancy, fault slip proceeds from steady state, to simple periodic, to complex periodic or aperiodic, eventually to seismic as W/h^* increases. We show that, in addition to parameters E and U that are directly related to the pore pressure evolution, W/h^* continues to be an important factor in determining the fault response.

3.1.1. Effect of W/h^*

[19] For the simplified spectral model shown in Figure 1, the average $b - a$ over W is $\langle b - a \rangle = 0.002$. We keep $W = 20 \text{ km}$ and $d_c = 40 \mu\text{m}$ in all simulations and vary $\bar{\sigma}_0$ to achieve a wide range of W/h^* . For example, $\bar{\sigma}_0 = 0.6 \text{ MPa}$ results in $W/h^* \approx 23.5$.

[20] For selected pairs of dilatancy parameters E and U , Figure 2 summarizes the maximum slip rate V_{\max} on the velocity-weakening fault ($0 \leq \xi \leq W$) during episodes of modeled SSEs and the recurrence period T_{cyc} as functions of W/h^* , compared to calculations without dilatancy. When pore pressure is assumed to be time-invariant (black solid dots), similar to the results of *Liu and Rice* [2007] and *Rubin* [2008], simple periodic oscillations with $V_{\max} = V_{pl}$ start to appear at $W/h^* \approx 3$, followed by “period doubling” oscillations (two dots at one W/h^*) for $W/h^* \gtrsim 16$. The difference between V_{\max} of two events in one period doubling

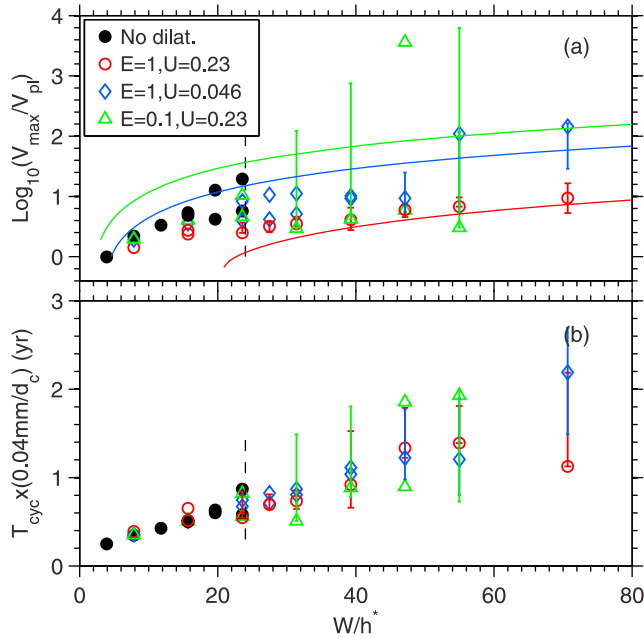


Figure 2. (a) Maximum slip velocity V_{\max} in the velocity-weakening zone (normalized by V_{pl}) and (b) recurrent period T_{cyc} as functions of W/h^* for simulation cases with (open symbols) and without (black solid dots) dilatancy. Vertical dashed line at $W/h^* \approx 24$ represents the “abrupt” jump from aseismic to seismic slip rates, defined without dilatancy. Pairs of dilatancy and drainage parameters are $E = 1$, $U = 0.23$ (red circles), $E = 1$, $U = 0.046$ (blue diamonds), and $E = 0.1$, $U = 0.23$ (green triangle). For these relatively small values of E and U , W/h^* from equation (18), as plotted here, is very similar to the adjusted values in equation (22). Maximum likelihood values of V_{\max} and T_{cyc} are determined for each case from selected interseismic time windows that are free of earthquake nucleation and postseismic relaxation effects. Error bars on each symbol represent the variational range (minimum to maximum) within the selected time window. Solid curves represent V_{\max} as a function of W/h^* , for pairs of (E, U) of corresponding colors, estimated as in equation (19).

episode increases with W/h^* . The vertical dashed line at $W/h^* \approx 24$ represents the “abrupt” jump from aseismic to seismic slip rates, which is close to that estimated by Rubin [2008] with $W/W = 5$ and a similar linear gradient in a/b .

[21] Open symbols represent calculations including dilatancy. We choose three sets of dilatancy and drainage parameters: $E = 1$, $U = 0.23$; $E = 1$, $U = 0.046$; and $E = 0.1$, $U = 0.23$, to investigate how different combinations of dilatancy and diffusion parameters affect the slow slip process. A general observation from all the dilatancy calculations in Figure 2 is that aseismic oscillations now exist over a much broader range of W/h^* . For all the three sets of parameters, except for two cases at $W/h^* \approx 47$ and 55 with $E = 0.1$ and $U = 0.23$, V_{\max} remains less than $10^3 V_{pl}$ up to $W/h^* \approx 70$, the largest in our calculation to maintain a resolution of $L_b/h > 3$, where h is the grid spacing ($L_b = (\mu' d_c)/b\bar{\sigma}_0$ is a characteristic nucleation size defined by Ampuero and Rubin [2008]; most simulations have the ratio L_b/h between 5 and 9). At $W/h^* < 23.5$, slow slip events

under of the influence of dilatancy appear as simple periodic or periodic doubling episodes, with small variations in V_{\max} and T_{cyc} . V_{\max} is slower than those without dilatancy; at $W/h^* = 23.5$, V_{\max} with $E = 1$ and $U = 0.23$ is nearly one order of magnitude smaller than the highest V_{\max} without dilatancy. At $W/h^* > 23.5$, V_{\max} and T_{cyc} continue to increase, with generally less periodicity and much greater variation range at each W/h^* .

[22] As shown in Appendix A (equations (A23) to (A26) and Figure A2), following an instantaneous velocity jump from V_1 (and initial state θ_i) to V_2 , the total fracture energy is dominated by the energy from pore suction for dilatancy parameter $E \gtrsim 1$ and drainage parameter $U \gtrsim 1$. Using the balance between pore suction dominated fracture energy and the mechanical energy release for a crack of width W governed by the rate and state friction at partially drained condition, we derived an analytical estimate of transients maximum slip rate as a function of parameters E , U , W/h^* and a/b

$$\frac{V_{\max}}{V_{ss}} \left[\ln \left(\frac{V_{\max}}{V_{ss}} \right) \right]^{-1} = \frac{1}{2EU} \left(1 - \frac{a}{b} \right) \frac{W}{h^*}. \quad (19)$$

Detailed derivation is in Appendix B. The solid curves in Figure 2a plot the estimate from equation (19) as functions of W/h^* , for pairs of (E, U) with corresponding colors to simulation cases and an average $a/b = 0.9412$. The prediction by equation (19) is generally consistent with the model results in the following two aspects. First, the decreasing slope of $\log_{10}(V_{\max}/V_{pl})$ with W/h^* agrees with the numerical simulations, despite the significant variations in the simulations exhibited by aperiodic events at large W/h^* . Second, at the same W/h^* , a smaller product of EU predicts a higher (or a higher range of) V_{\max}/V_{pl} . The deviation of model results from the analytical estimate can be due to several reasons, such as the approximation of fracture energy only from pore suction, especially for the $E = 0.1$, $U = 0.23$ case, and neglecting the contribution to the mechanical energy release from the continuous motion over $\xi > W$. Nevertheless, for conditions $E \gtrsim 1$ and $U \gtrsim 0.1$, equation (19) seems likely to provide a reasonable estimate of the maximum slip rate at large W/h^* (e.g., > 100) that, if to be calculated numerically, would require higher grid resolution (or a larger grid) and longer computation time than achieved in this study.

[23] Figures 3 and 4 compare the velocity and state evolution during modeled SSEs without and with dilatancy at $W/h^* = 23.5$. For the event under a constant pore pressure (without dilatancy), transient slip with velocity higher than V_{pl} starts to appear near the middle of the velocity-weakening zone, followed by an updip propagation which stops when reaching the locked segment. As shown in Figure 3, the slow slip event initiates at $\xi \approx 11.5h^*$ where the maximum slip speed is about $2V_{pl}$, and $\ln(V_{\max}\theta_i/d_c) \approx 2$. Slip steadily propagates (propagation speed v_r , relatively constant) to $\xi \approx 6h^*$ where $V_{\max} \approx 7V_{pl}$ and $\ln(V_{\max}\theta_i/d_c) \approx 5.6$. This steady propagation is followed by more rapid increases in V_{\max} and v_r until the front reaches $\xi \approx 1.5h^*$, where both properties are at maximum. V_{\max} and v_r then quickly decrease as the front approaches the locked region. Except for the first few snapshots before successive slip fronts

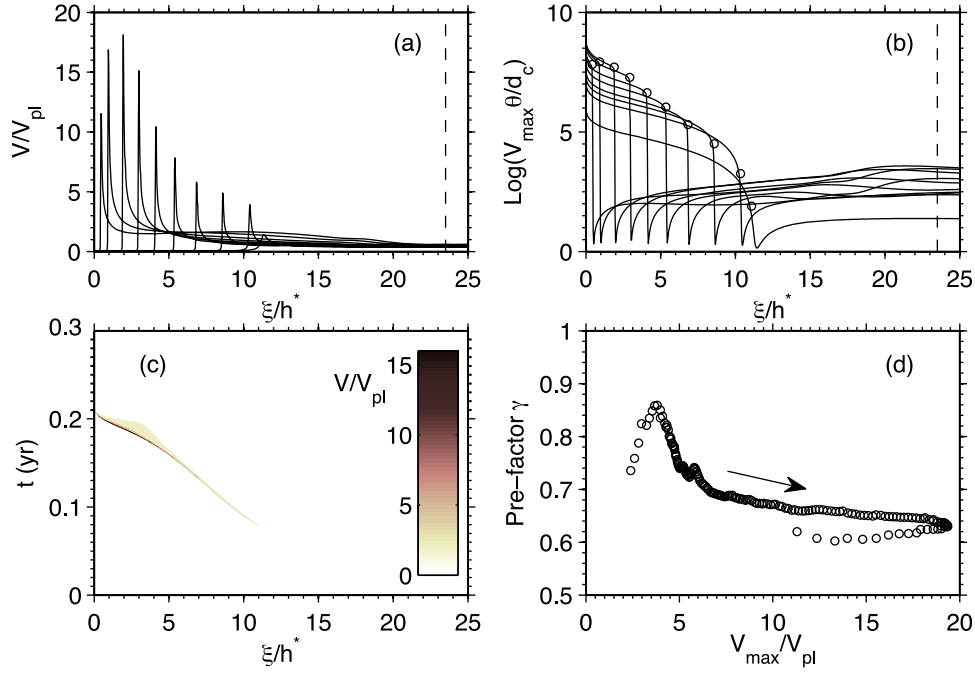


Figure 3. Snapshots of normalized (a) slip velocity V/V_{pl} and (b) state variable $\ln(V_{\max}\theta_i/d_c)$ during a modeled transient event without dilatancy. From right to left, snapshots are taken at $t \approx 0.075, 0.085, 0.109, 0.134, 0.154, 0.170, 0.181, 0.189,$ and 0.196 year (reference $t = 0$ in Figure 3c). Vertical dashed line denotes the friction stability transition from velocity weakening ($\xi/h^* \leq 23.5$) to velocity strengthening ($\xi/h^* > 23.5$). V_{\max} in Figure 3b is determined from the simulation at each snapshot. $d_c = 40 \mu\text{m}$. Open circles show the values of $\ln(V_{\max}\theta_i/d_c)$ for each snapshot, where θ_i is the state taken at 4 grid points ($\approx 0.115h^*$) ahead of the crack tip (maximum friction f). (c) Contour of V/V_{pl} as a function of time and distance along the fault. The darkest shade represents the propagation front of maximum slip velocity. (d) Prefactor $\gamma = (v_r/V_{\max})(\Delta\tau^{p-r}/\mu') \approx (v_r/V_{\max})(b\bar{\sigma}_0/\mu')\ln(V_{\max}\theta_i/d_c)$ variation as the slip front progresses. v_r is the slip propagation speed. Denser sampling rate is used in Figure 3d than in Figures 3a and 3b.

become self-similar (before reaching $\xi \approx 6h^*$), V_{\max} and v_r approximately follow a linear relation

$$\frac{v_r}{V_{\max}} = \gamma \frac{\mu'}{\Delta\tau^{p-r}}, \quad (20)$$

that was first obtained by *Ida* [1973] for a mode II elastodynamic rupture and recently confirmed in the context of slow dip-slip events for both along-strike [*Shibazaki and Shimamoto*, 2007] and along-dip [*Rubin*, 2008] propagations. *Ampuero and Rubin* [2008] pointed out that with $\Delta\tau^{p-r} \approx b\bar{\sigma}_0 \ln(V_{\max}\theta_i/d_c)$ this relation becomes

$$\frac{v_r}{V_{\max}} \approx \gamma \frac{\mu'}{b\bar{\sigma}_0} \frac{1}{\ln(V_{\max}\theta_i/d_c)}. \quad (21)$$

The prefactor γ is a coefficient of proportionality between the inverse of slip gradient v_r/V_{\max} and $\mu'/\Delta\tau^{p-r}$; γ is of order of unity. The initial state θ_i is usually taken at a few grid points ahead of the tip, but since there is little state evolution prior to the arrival of the peak stress the results are not very sensitive to this choice. Figure 3d shows the variation of prefactor γ (according to equation (21)) as a function of V_{\max}/V_{pl} during the slip propagation. The initial modest rise and drop in γ before V_{\max} reaches $\sim 7V_{pl}$ is due to the lack of self-similarity between successive slip fronts. For the updip accelerating propagation from $\xi = 6h^*$ to

$1.5h^*$ and the subsequent decelerating propagation to the locked region, the prefactor γ remains roughly a constant of 0.64, close to $\gamma \approx 0.6$ estimated for earthquake nucleation propagation with the ‘‘aging’’ law by *Ampuero and Rubin* [2008].

[24] For the event with fluid pressure controlled by pore compaction and dilatancy, we demonstrate the velocity and pore pressure evolution in a simulation case with representative parameters $E = 1$, $U = 0.23$ and $W/h^* = 23.5$. As shown in Figure 4, transient slip initiates in the velocity-weakening region closer to the locked segment than its no-dilatancy counterpart. The maximum velocity starts to exceed V_{pl} at $\xi \approx 7h^*$. The updip propagation first accelerates for a short distance until reaching a maximum velocity of $\sim 3.6V_{pl}$ at $\xi \approx 4.4h^*$, followed by a decelerating propagation toward the locked segment; at $\xi \approx 0.2h^*$, $V_{\max} \approx 1.2V_{pl}$. In the first few snapshots of the accelerating phase, the prefactor γ varies from ~ 0.52 to 0.68 (triangles in Figure 4e), which cannot be simply explained by the small increase in $\ln(V_{\max}\theta_i/d_c)$ as shown in Figure 4c. Rather, this large fluctuation is most likely due to the fact that self-similarity between successive slip fronts has not formed yet in this stage. During the decelerating phase, the slip fronts are approximately self-similar, and $\gamma \approx 0.6$, similar to the estimate for the no-dilatancy situation. Note from Figure 4c that there is some reduction in state θ prior to the arrival of the peak friction, as compared to the near-maximum θ_i for each

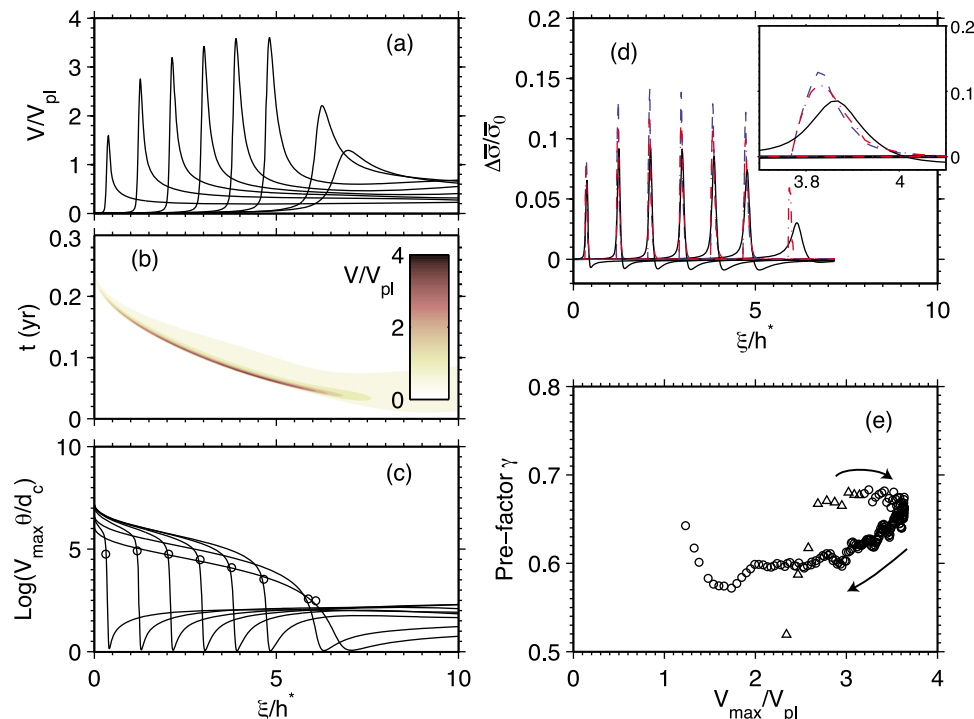


Figure 4. Snapshots of normalized (a) slip velocity V/V_{pl} , (c) state variable $\ln(V_{\max}\theta/d_c)$, and (d) effective normal stress change $\Delta\bar{\sigma}/\bar{\sigma}_0$ during a modeled transient event with dilatancy. From right to left, snapshots are taken at $t \approx 0.034$ (not shown in Figure 4d), 0.043, 0.063, 0.080, 0.100, 0.123, 0.151, and 0.193 year (reference $t = 0$ in Figure 4b). Model parameters are $W/h^* = 23.5$, $E = 1$, $U = 0.23$. Friction stability transition is at $\xi/h^* = 23.5$ (not shown here). Open circles show $\ln(V_{\max}\theta/d_c)$ for each snapshot, where θ_i is θ 4 grid points ($\approx 0.057h^*$) ahead of the crack tip. (b) Contour of V/V_{pl} . (d) Positive $\Delta\bar{\sigma}/\bar{\sigma}_0$ corresponds to pore pressure drop due to dilatancy. Black solid lines are from the simulation. Blue dashed lines are estimates from equations (A23) and (A25), with θ_i from the simulation, and red dot-dashed lines are estimated by directly integrating equation (A20). An enlarged view of a pore suction peak between $\xi/h^* = 3.7$ and 4.1 is shown at the top right. (e) Prefactor γ variation as the slip front progresses. Denser sampling rate is used in Figure 4e than in Figures 4a, 4c, and 4d.

(except the first a few) snapshot in Figure 3b. This is mainly due to the smaller V_{\max} and the less impulsive velocity jumps at such E and U conditions compared to those without dilatancy; calculation at a smaller $E = 0.1$ or a larger $W/h^* = 39.2$ (same other parameters) shows more instantaneous velocity jump and more abrupt reduction in θ as the crack tip arrives.

[25] The black solid line snapshots in Figure 4d demonstrate the pore pressure evolution accompanying the slow slip process. Positive and negative $\Delta\bar{\sigma}/\bar{\sigma}_0$ correspond to an increase (fluid pressure drop) and decrease (fluid pressure rise) in effective normal stress, respectively. The slip velocity increase induces transient fluid pressure drop followed by reequilibration to the ambient level. For $E = 1$ and an intermediate degree of drainage ($U = 0.23$) used here, the maximum nondimensional suction $\Delta\bar{\sigma}/\bar{\sigma}_0$ is ~ 0.1 ; $\Delta\bar{\sigma}/\bar{\sigma}_0$ would be between 0.2 and 0.3 if the fault zone is fully undrained, according to equation (12) with $\ln(V_2/V_1) \approx \ln(V_{\max}\theta/d_c)$ between 3.5 and 5.5. The duration of the transient pore suction at specific locations on the fault is controlled by the drainage parameter U . A larger U indicates that it takes a longer time for pore pressure to return to its ambient level. For $U = t_p/(d_c/V_{ss}) = 0.23$, as the sliding

velocity is only moderately (less than one order of magnitude) higher than V_{pl} ($\approx 4.35V_{ss}$), the characteristic pore pressure diffusion time is comparable to the time for friction to evolve to steady state. Therefore, in Figures 4a and 4d, for each point on the fault the duration of transiently $\Delta\bar{\sigma} > 0$ approximately corresponds to the duration when $V > V_{ss}$. Blue dashed lines represent the analytic estimate from equations (A23) and (A25). Red dashed lines are the solution by numerically integrating equation (A6), where $V_2 (= V_{\max})$ and θ_i are from the simulation at each snapshot. Their reasonable agreement with the simulation results suggests that our analytic estimates of pore pressure and shear stress evolution following an instantaneous velocity jump (Appendix A) can be used to approximately describe the slow slip process with dilatancy.

3.1.2. Effects of U and E

[26] Figure 5 shows the variation of maximum slip velocity on the velocity-weakening part and recurrence period with U ($E = 1$ fixed) and E ($U = 0.23$ fixed), respectively, at $W/h^* = 23.5$. For $U \ll 1$, fluid pressure quickly reequilibrates with the ambient level and thus the fault response approaches that of the no-dilatancy situation. In Figure 5a, the smallest $U = 0.0023$ case produces period

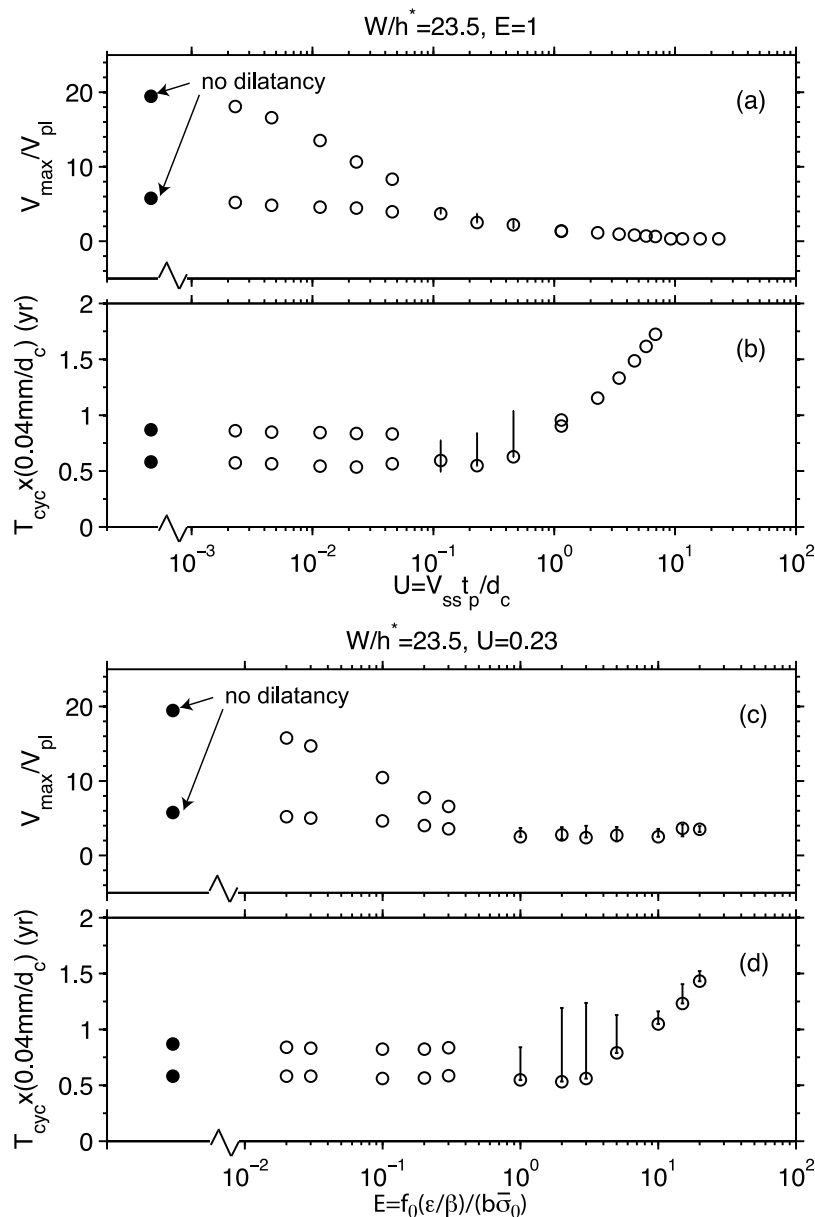


Figure 5. (a, b) Maximum slip velocity V_{\max}/V_{pl} on the velocity-weakening fault and recurrent period T_{cyc} variation with the drainage parameter $U = V_{ss} t_p / d_c$ ($E = 1$ fixed). (c, d) V_{\max}/V_{pl} and T_{cyc} variation with the dilatancy parameter $E = f_0(\epsilon/\beta)/(b\bar{\sigma}_0)$ ($U = 0.23$ fixed). $W/h^* = 23.5$. The scaling of T_{cyc} with d_c makes it possible to label the recurrence period axis with the factor $0.04 \text{ mm}/d_c$ so that the solutions can be interpreted for other choices of d_c . No-dilatancy results are also plotted in solid black circles (most left in each panel) for comparison.

doubling aseismic sequences, with the high and low velocities at $18V_{pl}$ and $5.2V_{pl}$ and recurrence periods of 0.86 and 0.57 year, respectively. These are very close to the velocities of $19V_{pl}$ and $5.7V_{pl}$ and recurrence periods of 0.87 and 0.58 year for the same $W/h^* = 23.5$ but without dilatancy. As U increases toward 1, the average V_{\max} decreases while the recurrence period remains relatively constant. This behavior can be explained by considering the amplitude and duration of pore suction and the following recovery stage. As U increases from the smallest 0.0023 to 0.23, the pore suction becomes larger and lasts longer. V_{\max} is smaller when the near-tip pore suction is larger. But smaller V_{\max}

also results in a longer duration for the slow event, because that duration is tied to the time it takes to propagate up dip to the locked zone. From equation (20) the propagation speed is roughly proportional to V_{\max} , so that the total slip during the slow event is only weakly dependent upon V_{\max} . When the slip per cycle is dominated by that accumulated during the slow event, this implies the slip per cycle, and hence the duration of the cycle, is also only weakly dependent upon V_{\max} .

[27] For $U \gg 1$, the fault zone is nearly undrained so that pore suction remains for a much longer duration than the state evolution time. V_{\max} approaches the steady state

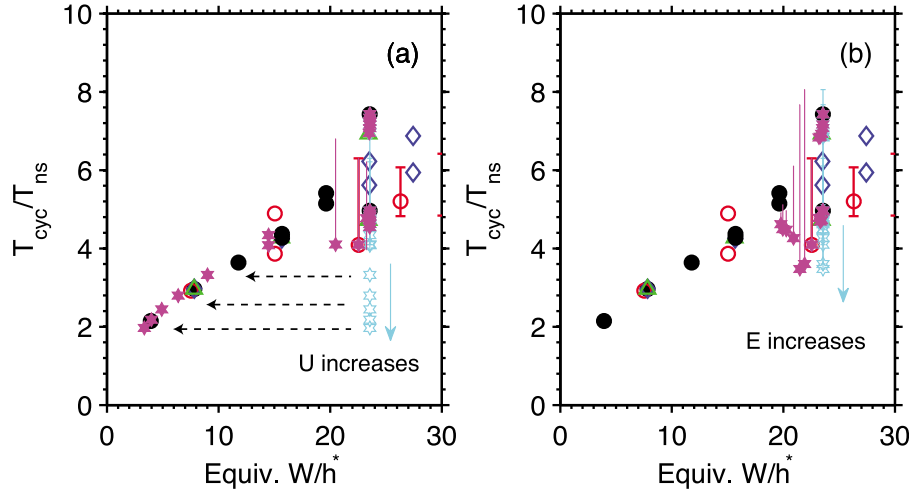


Figure 6. (a) Recurrence period T_{cyc} normalized by the neutral stability period $T_{ns}(E, U, a/b)$ versus W/h_{dilat}^* (equivalent W/h^*) according to equation (22), for simulation cases in Figure 2a ($W/h^* < 30$; same symbol legend) and cases in Figure 5b (open cyan hexagrams, before adjustment). Decreasing T_{cyc}/T_{ns} from ~ 4 to 2 corresponds to increasing U from ~ 1 to 10 in Figure 5b. Solid magenta symbols are the same cases but plotted versus the adjusted W/h^* . (b) Same as in Figure 6a, but for simulation cases in Figure 2a ($W/h^* < 30$) and cases in Figure 5d (open cyan hexagrams). Variation of T_{cyc}/T_{ns} with E is relatively smaller than that with $U \gtrsim 1$. The adjustments in W/h^* (solid magenta symbols) are smaller too.

velocity of $V_{ss} \approx V_{pl}/3$ at $\xi = W$, as shown in Figure 5a. In this limit, slip velocity as a function of time fluctuates in a near-sinusoidal shape, in contrast to velocity peaks concentrated in a time period much shorter than the recurrence interval for $U \ll 1$. Thus, T_{cyc} is expected to approach the neutral stability period T_{ns} (equation (C5)), which was derived by *Segall et al.* [2010] as a function of parameters E , U and a/b . T_{ns} demonstrates significant increase for $U > 1$, as shown in Figure C1a with $E = 1$ and $a/b = 0.9412$.

[28] Based on *Ruina's* [1983] results for a single-degree-of-freedom spring slider, *Rubin* [2008] proposed that the slip per cycle in continuum models of episodic slow slip was approximately the slip per cycle at neutral stability, plus a monotonically increasing function of W/h^* . We can express this cumulative slip during a SSE cycle as a recurrence interval, simply by dividing the slip by the steady state velocity V_{ss} at a representative point within W (here at $\xi = W/2$). However, to interpret the current simulations in this way we need to account for dilatancy induced changes to both the critical stiffness and the slip per period at neutral stability. Using the linearized stability analysis results by *Segall and Rice* [1995] and *Segall et al.* [2010] and the proportionality

$$\frac{W/h_{dilat}^*}{W/h^*} = \frac{k_{cr}^{dilat}}{k_{cr}} = \hat{K}_{cr}(E, U, a/b), \quad (22)$$

we calculated the equivalent W/h_{dilat}^* for all the simulation cases in Figures 2 and 5b. See Appendix C for equations of the critical stiffness k_{cr}^{dilat} and neutral stability period T_{ns} under dilatancy. The normalized recurrence period T_{cyc}/T_{ns} is plotted versus the adjusted W/h_{dilat}^* in Figure 6a. For the cases from Figure 2a, the adjustments in W/h^* are very small, as can be seen from the slight shifts from their original values, due to the choices of $U < 1$ for all three

groups. By contrast, the cases from Figure 5b, all aligned at their original $W/h^* = 23.5$, show significant adjustments especially for those with $U > 1$. At $U \approx 7$, the adjusted $W/h_{dilat}^* \approx 3.3$ is only 14% of its original value. After the adjustment, the relation between T_{cyc}/T_{ns} and W/h_{dilat}^* for U over three orders of magnitude agrees very well with the trend defined by the no-dilatancy and limited selections of (E, U) pair simulations, as well as with the trend for both the “aging” law and “slip” law simulations of *Rubin* [2008] using various values of W/W' and distributions of a/b . A similar trend was also found for dilatancy coupled with the “slip” law [*Segall et al.*, 2010]. Such an increase of normalized period with W/h_{dilat}^* is possibly due to the increase in time for the slow slip to propagate through the velocity-weakening region.

[29] The effects of parameter E ($U = 0.23$ fixed) are similar to that of parameter U . As shown in Figures 5c and 5d, for $E \ll 1$, both V_{max} and T_{cyc} approach the values without dilatancy because the pore suction is negligible compared to the initial $\bar{\sigma}_0$. As E increases toward 1, the average V_{max} decreases as higher pore suction is induced by larger porosity changes, while the recurrence period remains relatively constant due to the compensating effects of smaller velocity and longer sliding duration. For $U = 0.23$ and $a/b = 0.9412$, the neutral stability period T_{ns} moderately increases for $E > 1$ (Figure C1b), which may explain the slight increase in T_{cyc} when the fault response approaches that at neutral stability condition. In contrast to the rapid decrease of k_{cr}^{dilat} for $U > 1$, the variation of critical stiffness with E is very small (Figure C1b). As a result, the adjustments in W/h^* are relatively small as shown in Figure 6b. The adjusted relation between T_{cyc}/T_{ns} and W/h_{dilat}^* also agrees with the trend defined by the no-dilatancy and limited choices of (E, U) cases.

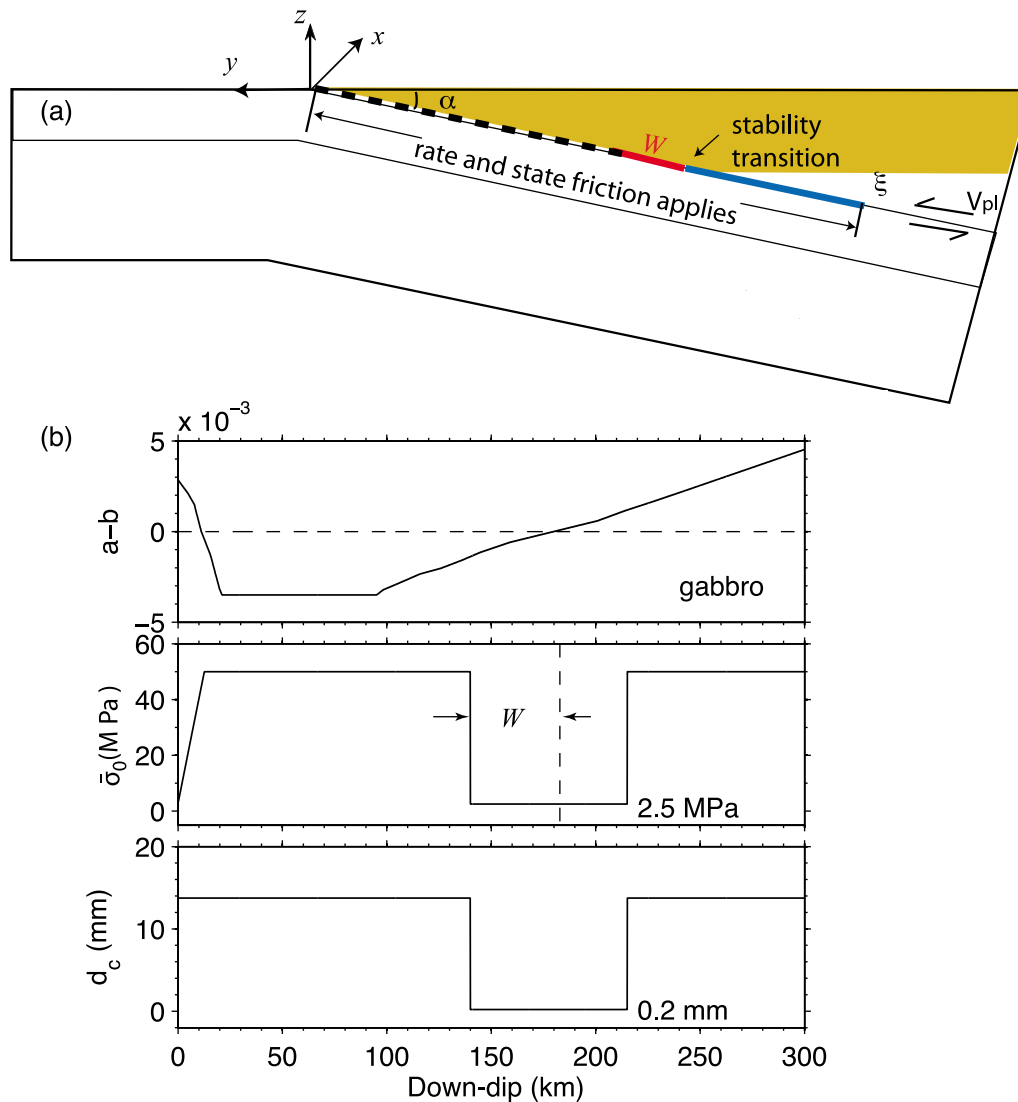


Figure 7. (a) Two-dimensional subduction fault model. The thrust fault is simulated by a planar frictional interface dipping at 12° in an elastic half-space. ξ is distance along down-dip direction. Rate and state friction applies between $0 \leq \xi \leq 300$ km. Fault is loaded by a constant plate rate $V_{pl} = 37$ mm yr $^{-1}$ down-dip from $\xi = 300$ km. Properties are uniform along the strike direction x (perpendicular to y - z plane). Bold red line represents the velocity-weakening fault of width W updip from the stability transition under low effective normal stress. (b) Friction parameter a - b , initial effective normal stress $\bar{\sigma}_0$, and characteristic evolution distance d_c down-dip distributions. Temperature-dependent a - b from *He et al.* [2007] experiments are mapped to be depth-dependent using a Cascadia thermal model by *Peacock et al.* [2002]. Lower friction stability transition is at ~ 180 km.

3.2. The 2-D Subduction Fault Model

3.2.1. Geometry and Model Parameters

[30] In this section, we investigate the effect of dilatancy and pore compaction on a 2-D fluid-infiltrated subduction fault. The fault model is set up similarly to that of *Liu and Rice* [2007, 2009], and is summarized here in Figure 7. We simulate the thrust fault by a planar frictional interface in an elastic half-space, with a 2-D plane strain assumption. As a simple representation of the northern Cascadia shallow subduction geometry, the thrust fault dips at a constant angle of 12° ; ξ now starts from the trench and aligns with the down-dip direction. Rate and state-depen-

dent friction is applied on the interface from $\xi = 0$ to $\xi = 300$ km. Further down-dip the fault is loaded by a constant rate $V_{pl} = 37$ mm yr $^{-1}$. Friction parameters a , a - b and d_c are functions of the down-dip distance ξ , and are invariant with time. Friction experimental data for gabbro have recently been reported by *He et al.* [2007]. A tentative application of the gabbro data, as the first set available for a reasonable representation of the igneous rocks of the seafloor, to a Cascadia-like subduction fault model can produce slow slip events with surface deformation similar to those observed by GPS stations, while models using the wet granite data [*Blanpied et al.*, 1998], which, for lack of a suitable alternative, has been the basis for most previous calculations,

result in a very poor fit [Liu and Rice, 2009]. Thus, in this paper, we apply the He *et al.* [2007] gabbro friction data in the 2-D fault model. Using a Cascadia subduction zone thermal profile [Peacock *et al.*, 2002], the temperature-dependent a - b is converted to be depth-dependent as shown in Figure 7b (top). See Liu and Rice [2009] for detailed discussions of the choice of a - b and application in the 2-D subduction fault model. In the velocity-weakening regime, a - b remains as a constant of -0.0035 to ~ 95 km, followed by a gradual transition to velocity strengthening at ~ 180 km. Parameter a - b is about 0.005 at the downdip end of the modeled fault $\xi = 300$ km. Direct effect a is assumed to increase linearly with the absolute temperature: $a = 5.0 \times 10^{-5}(T + 273.15)$, following an Arrhenius activated process at asperity contacts on the sliding surface [Rice *et al.*, 2001]. Parameter a is also converted to be depth-dependent using the Peacock *et al.* [2002] thermal profile. For simplicity, we consider the elastic effect of slip on altering only the shear stress, and variation in effective normal stress $\bar{\sigma}$ being the result only of fluctuation in pore pressure p . The static normal stress change is much smaller than the shear stress change, due to a uniform slip on the 2D subduction fault at depth of slow slip events. A few calculations in our previous studies with inclusion of the elastic effect of slip on the normal stress gave insignificantly different results [Liu and Rice, 2007; Rubin, 2008].

[31] The downdip distribution of the initial effective normal stress $\bar{\sigma}_0$ is determined following the discussion of along-dip elevated fluid pressure by Liu and Rice [2009], and an example is shown in Figure 7b (middle). Near the surface and in most part of the seismogenic zone, pore pressure p is assumed to be the maximum between the hydrostatic pressure $10[\text{MPa km}^{-1}] \times z$ and $28[\text{MPa km}^{-1}] \times z - 50$ MPa. The low effective normal stress zone extends some distance updip (W) and downdip from the friction stability transition, approximately consistent with the seismically inferred depth range of near-lithostatic fluid pressure in northern Cascadia [Audet *et al.*, 2009]; $\bar{\sigma}_0$ resumes to 50 MPa further downdip to 300 km.

[32] Similar to that in the simplified spectral model, W/h^* as defined in equation (18) is an important parameter that determines whether the system can produce self-sustained aseismic oscillations. $\langle b - a \rangle$ is the average $b - a$ over W . For the a - b distribution shown in Figure 7b, model parameters W , $\bar{\sigma}_0$ and d_c in the low effective normal stress zone are related via equation (18). We first choose the depth range of low $\bar{\sigma}_0$ zone to be consistent with the depths of metamorphic dehydration reactions encountered by the top of the northern Cascadia subduction slab, and in a reasonable agreement with seismically estimated extent of near-lithostatic p region. That is a few tens of kilometers updip and downdip from the stability transition. For each fixed W , $\langle b - a \rangle$ is thus determined. $\bar{\sigma}_0$ and d_c are then varied accordingly to result in a range of W/h^* that allow quasiperiodic aseismic events. On the rest of the fault, d_c is uniformly

$$d_c = \frac{\pi(b - a)_{\max} \bar{\sigma}_0 h_0^*}{2\mu'} \quad (23)$$

where $(b - a)_{\max} = 0.0035$ is the maximum velocity-weakening value, and h_0^* is a fixed factor (16 in all calculations) times the computational grid size h to assure com-

puted results are free from grid discretization effect. In the example shown in Figure 7b, $W = 40$ km, $d_c = 0.2$ mm in the $\bar{\sigma}_0 = 2.5$ MPa zone such that $W/h^* \sim 16$. $d_c = 13.74$ mm elsewhere on the fault. Modeling results applying the gabbro friction data to a Cascadia-like subduction fault have been presented in our previous study [Liu and Rice, 2009] and are briefly summarized in section 3.2.2.

3.2.2. The 2-D Results Without Dilatancy

[33] A general fault response to the above loading conditions and model parameters is that mega-thrust earthquakes rupture the entire seismogenic zone every few hundred years, and quasiperiodic aseismic transients, mostly within the low $\bar{\sigma}_0$ zone, appear every few years in the interseismic period.

[34] Four groups of calculations with $W = 35, 40, 50$ and 55 km are performed in the range of $W/h^* = 6$ to 16 , which allows spontaneous aseismic transients. Three representative properties of transients: maximum slip velocity V_{\max} , slip δ at the center of W accumulated when V_{\max} exceeds $2V_{pl}$, and recurrence period T_{cyc} , vary significantly for a wide spectrum of choices of W , low $\bar{\sigma}_0$ and d_c . The general trend is that all three properties increase with W/h^* , as shown in Figure 9 (solid gray symbols), as has also been observed from calculations using the wet granite friction data [Liu and Rice, 2009]. At the same W/h^* , the variation range of the three properties with different choices of W are relatively large, compared to those using the granite data, because the velocity-weakening a - b follows a gradual increase to neutral stability over the entire width of W . Detailed discussions of modeled transient properties and comparison of calculated surface deformation to GPS observations in northern Cascadia are given by Liu and Rice [2009].

3.2.3. The 2-D Model Results With Dilatancy

[35] The introduction of E and U adds to the vast parameter space that needs to be explored in modeling the properties of slow slip events. In this paper, we use a constant $W = 40$ km, which, in combination with appropriate choices of $\bar{\sigma}_0$ and d_c , has been shown to produce surface deformations in reasonable agreement with GPS observations in northern Cascadia [Liu and Rice, 2009]. Furthermore, with the knowledge that fault response approaches the no-dilatancy situation at $U \ll 1$ and steady state at $U \gg 1$, we focus on the intermediate degree of drainage, that is, U of order unity.

[36] Figure 8 shows sequences of slow slip events for 100 years within the interseismic period, using parameters $W = 40$ km, $\bar{\sigma}_0 = 2.5$ MPa, $d_c = 0.2$ mm (thus $W/h^* \sim 16$) and $\epsilon/\beta = 0.1$ MPa (thus $(\epsilon/\beta)/\bar{\sigma}_0 = 0.04$ and $E \approx 0.63$ in the low $\bar{\sigma}_0$ zone). Two megathrust earthquakes occur at ~ 224 yr and 655 yr, with the maximum seismic velocity about 0.1 m s^{-1} (not shown here). In the interseismic period, V_{\max} oscillates between V_{pl} and the peak aseismic rate of $\sim 20V_{pl}$, which is nearly 3 orders of magnitude smaller than its counterpart without dilatancy. Figure 8 (middle) shows slip δ at the center of W accumulated during each episode when V_{\max} exceeds $2V_{pl}$. Figure 8 (bottom) shows the recurrence period T_{cyc} , defined as the interval between two successive events when V_{\max} reaches the peak value. The moderate variations in δ and T_{cyc} are due to the interseismic strength evolution, including evolution of pore pressure, in the low $\bar{\sigma}_0$ zone and updip in the nearly locked zone. From the selected interseismic time windows that are free of the

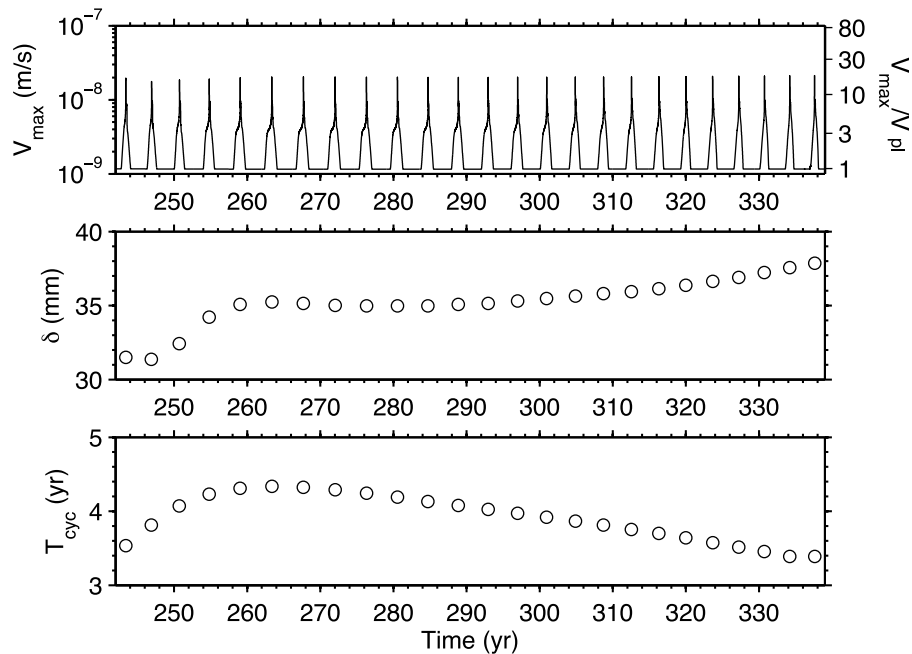


Figure 8. Spontaneous short-period transients in a 100 year interseismic period, using gabbro friction data. Initial $\bar{\sigma}_0$ and d_c distributions are shown in Figure 7b. In the low $\bar{\sigma}_0 = 2.5$ MPa zone, dilatancy parameter $\epsilon/\beta = 0.1$ MPa (thus, $(\epsilon/\beta)/\bar{\sigma}_0 = 0.04$), corresponding to open red diamond at $W/h^* \sim 16$ in Figure 9), drainage parameter $U = 0.23$. (top) Maximum slip rate on the fault. (middle) Slip accumulated during each transient event when $V_{\max} > 2V_{pl}$ at the center of velocity-weakening low $\bar{\sigma}_0$ zone. (bottom) Recurrence interval.

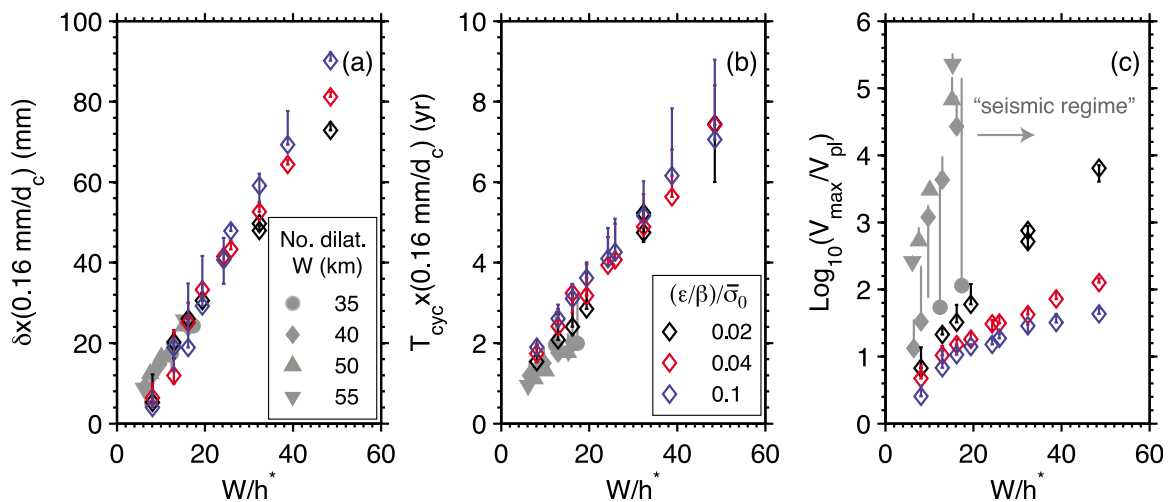


Figure 9. Exploration in the parameter space, using gabbro friction data, shows that (a) cumulative slip, (b) recurrence interval, and (c) maximum velocity of modeled SSEs all increase with W/h^* . Solid gray symbols represent cases using $W = 35, 40, 50,$ and 55 km, respectively, without dilatancy effect for reference. Open diamond symbols are cases using a fixed $W = 40$ km, drainage $U = 0.23$, and different dilatancy parameters $(\epsilon/\beta)/\bar{\sigma}_0 = 0.02$ (black), 0.04 (red), and 0.1 (blue), corresponding to an average $E = 0.31, 0.63,$ and 1.57 , respectively, in the low $\bar{\sigma}_0$ zone. $\delta, T_{cyc},$ and V_{\max} are plotted versus the original W/h^* (equation (18)), because adjustments based on equation (22) are very small for the E and U values used here; $(W/h_{dilat}^*)/(W/h^*) = 0.985, 0.974$ and 0.942 , respectively, for the three cases. Variational range in $\delta, T_{cyc},$ and V_{\max} for each calculation, as shown in Figure 8, are represented by error bars. δ and T_{cyc} are labeled such that they can also be interpreted for other choices of d_c .

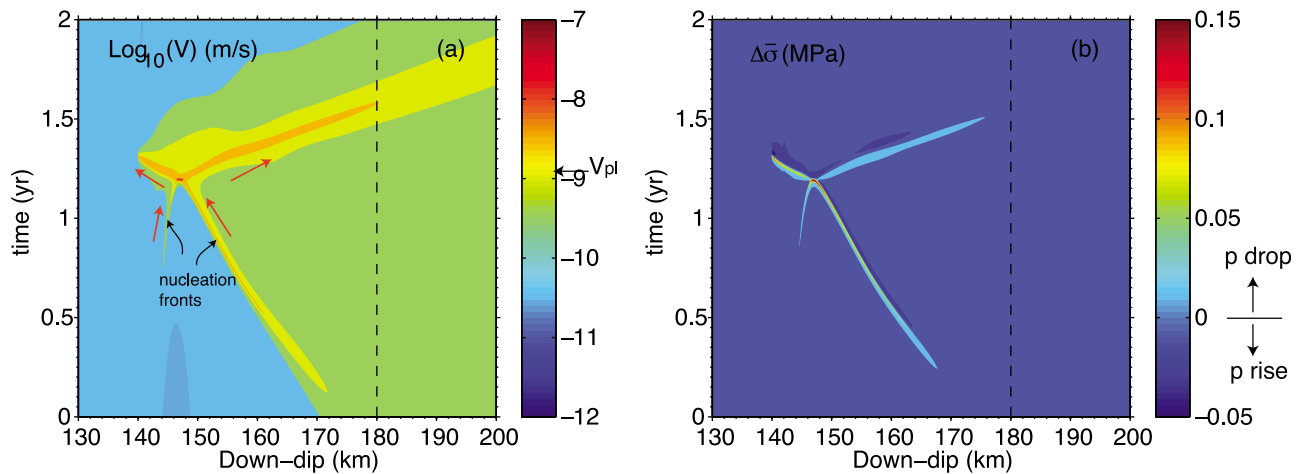


Figure 10. (a) Slip velocity $\log_{10}(V)$ in m s^{-1} and (b) pore pressure, represented by $\Delta\bar{\sigma} = -(p - p_0)$ in MPa, during a modeled transient event, using $W = 40$ km, low $\bar{\sigma} = 2.5$ MPa, and $d_c = 0.2$ mm ($W/h^* \sim 16$). Dilatancy-related parameters are $U = 0.23$, $(\epsilon/\beta)/\bar{\sigma}_0 = 0.04$ ($E = 0.63$) in the low $\bar{\sigma}_0$ zone and $\epsilon/\beta = 0.2$ MPa at depths with high $\bar{\sigma}_0 = 50$ MPa. Vertical dashed line points the position of velocity weakening to strengthening stability transition.

earthquake nucleation and postseismic relaxation effects, we make the histograms of δ and T_{cyc} , identify their maximum likelihood values, and record the maximum and minimum of each property as its variation range shown by error bars in Figure 9.

[37] Using constant $W = 40$ km and $U = 0.23$, three groups of calculations with $(\epsilon/\beta)/\bar{\sigma}_0 = 0.02, 0.04$ and 0.1 in the low $\bar{\sigma}_0$ zone, corresponding to an average $E = 0.31, 0.63$ and 1.57 respectively, are summarized in Figure 9. Outside the low $\bar{\sigma}_0$ zone, a uniform $\epsilon/\beta = 0.1, 0.2$ and 0.5 MPa is used, respectively, so that the behavior of larger earthquakes is roughly the same. For reference, solid gray symbols represent results from calculations without dilatancy; for which spontaneous aseismic events are present within the range $W/h^* \sim 6$ to 16 [Liu and Rice, 2009]. For each group of $(\epsilon/\beta)/\bar{\sigma}_0$ (constant E), $\bar{\sigma}_0$ and d_c are varied according to equation (18) to result in $W/h^* \approx 8, 12.8 \dots 48$. Here, we use the original “drained” definition for W/h^* because the adjustments due to the introduction of dilatancy (equation (22)) are very small; $(W/h_{dilat}^*)/(W/h^*) = 0.985, 0.974$ and 0.942 , respectively, for the three cases of $(\epsilon/\beta)/\bar{\sigma}_0$. Similar to that shown in Figure 6, the cumulative aseismic slip δ and recurrence period T_{cyc} both approximately follow the increasing trends with W/h^* as defined in the no-dilatancy situation. The lower limit of W/h^* for the onset of spontaneous aseismic transients is slightly larger in the dilatancy situation due to its stabilizing effect. Dramatic differences exist in the maximum velocity reached during transients. For example, without dilatancy V_{max} quickly approaches seismic rate ($>10^{-3} \text{ m s}^{-1} \sim 10^6 V_{pl}$) as W/h^* increases toward 16, while V_{max} is less than $10^2 V_{pl}$ at the same W/h^* with dilatancy, for the choices of E and U in this study. The stabilizing effect is more prominent as W/h^* increases beyond the no-dilatancy boundary; at $W/h^* \sim 32$, $V_{max} \approx 10^{2.8} V_{pl}$ for $(\epsilon/\beta)/\bar{\sigma}_0 = 0.02$, and $V_{max} \approx 10^{1.3} V_{pl}$ for $(\epsilon/\beta)/\bar{\sigma}_0 = 0.1$. For the small $(\epsilon/\beta)/\bar{\sigma}_0 = 0.02$, $\log_{10}(V_{max}/V_{pl})$ approximately follows a linear increasing trend with W/h^* , which is supported by $V_{max} \sim 5 \times 10^{-5} \text{ m s}^{-1} \approx 10^{4.5} V_{pl}$ at $W/h^* \sim 64$

(not shown in Figure 9). Following such a linear trend, seismic rate can be reached at $W/h^* \sim 80$. The rate at which V_{max} increases with W/h^* becomes smaller for larger $(\epsilon/\beta)/\bar{\sigma}_0$. This trend is similar to the prediction by equation (19). However, besides various complicated factors such as the influence from earthquakes, the nonuniform distributions of a/b and different choices of E in the high and low $\bar{\sigma}_0$ zones, the most important reason that slip velocities here are larger than those in Figure 2 is the merge of the updip and downdip propagating nucleation fronts when there is creep in the updip high $\bar{\sigma}_0$ zone [Liu and Rice, 2007; Rubin, 2008]. Here, nucleation fronts refer to slip fronts before they merge and reach the maximum slip rate; see Figure 10a. Due to such complications, we do not attempt to compare the simulation results for the 2-D subduction fault model to the analytical prediction.

[38] Figure 10 illustrates the slip velocity and pore pressure evolution during a modeled transient event, with dilatancy parameters $U = 0.23$, $(\epsilon/\beta)/\bar{\sigma}_0 = 0.04$ in the low $\bar{\sigma}_0 = 2.5$ MPa and $d_c = 0.2$ mm zone. Only the depth range involved in the transient slip is plotted. The friction stability transition is at downdip 180 km, and the low $\bar{\sigma}_0$ zone extends from 140 to 215 km. As shown in Figure 10a, a major nucleation front first appears at ~ 170 km and migrates updip within the low $\bar{\sigma}_0$ zone before the maximum velocity is reached. A secondary nucleation front, driven by the creep in the updip seismogenic zone, with smaller velocity and slower downdip migration speed, shows up when the major nucleation front has reached ~ 155 km. After the two nucleation fronts merge and reach a maximum velocity of $\sim 2.5 \times 10^{-8} \text{ m s}^{-1}$, slip propagates in both updip and downdip directions along the fault. The updip propagation continues for a short distance before it encounters the abrupt increase to $\bar{\sigma}_0 = 50$ MPa; meanwhile the downdip propagation extends to the stability transition before the velocity decreases to around V_{pl} . Both the propagation speed and sliding velocity are comparable along the updip and downdip directions, suggesting approximately similar stress drops associated with the slow slips.

The general feature of pore pressure variation, represented by $\Delta\bar{\sigma} = -(p - p_0)$ in Figure 10b, is very similar to those of slip velocity evolution in Figure 10a as the change in p is directly related to the change in state variable by equation (10). Along the major nucleation front, pore pressure drops as the fault slips faster due to the increased porosity and insufficient fluid supply in the state evolution time scale to refill the pores. As the nucleation front passes by and velocity returns to the level near V_{pb} , we observe a transient phase of pore pressure rise of a smaller amplitude because the magnitude of the velocity drop is smaller than that of the velocity rise associated with the nucleation front, assuming both processes take place in comparable time scales. After the maximum velocity is reached, pore pressure drop and rise are of the similar amplitude (≤ 0.05 MPa) along the front that propagates downdip, as a result of similar magnitude of velocity increase and subsequent decrease.

4. Discussion

[39] An important simplification in the above analysis is “membrane diffusion,” which approximates the fault-normal fluid pressure diffusion term $c(\partial^2 p / \partial \zeta^2)$ by a linear gradient between pressures on the fault and of the ambient rock $(p_0 - p)/t_p$. The approximation applies when the slipping interface is bordered by a low permeability layer surrounded by rock mass of constant ambient pore pressure, and the slip time is long compared to the diffusion time across that layer. While such a simplification reduces computation time and thus allows more extensive exploration in the parameter space, a more accurate description of the dilatancy effects on aseismic transients requires full solutions to the homogeneous diffusion equation (7). *Segall et al.* [2010] used a finite difference scheme to solve the fault-normal diffusion equation, coupled to the rate and state friction (“slip” evolution law) and elasticity equations. Neglecting the radiation damping term, they found that the solutions are dependent on the following nondimensional parameters: a/b , W/h^* (drained), f_0/b and a dilatancy efficiency parameter E_p (higher E_p corresponds to stronger dilatancy effect). Comparing results to the “membrane diffusion” model, they concluded that the homogeneous diffusion solution does not fundamentally change the dilatancy effect in stabilizing slip to aseismic transients.

[40] Rate and state fault models with depth-variable friction parameters and slow tectonic loading predict earthquake nucleation in the velocity-weakening zone close to the friction stability transition [e.g., *Lapusta et al.*, 2000; *Lapusta and Rice*, 2003]. Coseismic rupture sweeps the entire velocity-weakening zone and slightly into the adjacent velocity-strengthening zone. These conventional pictures may change when fluid pressure evolution is coupled into the system. We have shown in section 3.2.3 that dilatancy-strengthening can result in aseismic slip events in the otherwise seismic regime (Figure 9). Note that events in the “seismic regime” refer to episodic small earthquakes with coseismic rupture mostly limited to the low effective normal stress zone, usually within a few tens of kilometers around the friction stability transition [*Liu and Rubin*, 2010]. Thus, it remains to be explored whether the same stabilizing mechanism can also effectively prevent megathrust earthquake

nucleation, or in other words, under what conditions the occurrence of episodic slow slip events is indicative of megathrust nucleation. Our preliminary simulation cases suggest that, for sufficiently undrained fault segments with dilatancy parameter $E > 1 - a/b$ and $\bar{\sigma}_0$ of a few megapascals, megathrust earthquakes do fail to initiate where episodic SSEs are present. Instead, the nucleation takes place in the updip region at much higher $\bar{\sigma}_0$. These preliminary calculations were performed considering only the dilatancy-strengthening mechanism with “membrane diffusion.” While shear heating induced thermal pressurization can be reasonably neglected in the analysis of slow slip events due to the associated low heat generation rate, this weakening mechanism needs to be incorporated in the calculation of slip in major fault zones saturated with pore fluids and sliding near or at seismic rates (e.g., at late stages of earthquake nucleation, coseismic rupture and postseismic relaxation). We expect more complicated fault responses with the addition of fluid thermal pressurization, as some of the nucleation attempts in the low $\bar{\sigma}_0$ zone suppressed in the models in this work may be revived by the weakening effect.

[41] On the other end of an earthquake rupture spectrum is where it stops. Can the occurrence of SSEs be of any indication? Answering this question is of practical interest to seismic hazard assessment in populated regions such as the Pacific Northwest. In SW Japan, SSEs and nonvolcanic tremors seem to occur downdip from, but may not abut, the rupture areas of the 1944 Tonankai and 1946 Nankai earthquakes [*Obara*, 2002; *Ide et al.*, 2007]. In northern Cascadia where no great subduction earthquakes have been recorded in written history, decadal-scale geodetic observations can be modeled by assuming complete interseismic locking at shallow depths, with a broad zone of downdip transition from locking to full slip. Modest variations exist in different studies and for different along-strike sections [*Dragert et al.*, 1994; *Hyndman and Wang*, 1995; *Wang et al.*, 2003; *McCaffrey*, 2009]. A revised 3-D Cascadia dislocation model by *Wang et al.* [2003] predicts an effective transition zone width about twice the width of the locked zone. The depth of free sliding arguably coincides with the onset of slow slip events, assuming the slip events recover all the slip deficits in the long run. Taking the friction parameter distribution in this study and assuming that the occurrence of spontaneous episodic SSEs involves velocity-weakening friction, part of the broad transition zone should be frictionally unstable ($a - b < 0$) but can slip aseismically during a megathrust rupture. That is, a megathrust downdip rupture may stop before reaching the SSEs depth. Another possibility is the presence of small velocity-weakening patches embedded in the velocity-strengthening zone near the downdip end of the geodetically inferred transition zone, due to fault material property changes. Nevertheless, inclusion of fault gouge dilatancy appears to be a promising mechanism for the existence of a “gap” between megathrust rupture and slow slip. In our conceptual model, near-lithostatic fluid pressure is broadly present on the plate interface below the full locking depth. The lower part (around friction stability transition) of this high fluid pressure zone can accelerate episodically to slow slip events, while the upper part is more stabilized by a stronger dilatancy-strengthening effect. Further updip the fault is under much higher $\bar{\sigma}_0$ where megathrust earthquakes can nucleate.

Coseismic rupture may be stopped or damped as it propagates into the more stabilized region. Study of the proposed conceptual scenario in a Cascadia-like subduction fault model is under progress.

5. Conclusion

[42] This study analyzes frictional and hydraulic conditions for spontaneous aseismic deformation transients on a fluid-infiltrated fault including dilatancy and pore compaction in the framework of rate- and state-dependent friction, with the “membrane diffusion” approximation. Using a simplified fault model which is locked at one side and forced to slip at a constant rate at the other side (the locked and forced segments are much longer than the part where rate and state friction applies), we found that the incorporation of dilatancy enables aseismic transients beyond the aseismic-seismic boundary that is defined in the absence of dilatancy. The parameter W/h^* , ratio between the width of the fault subject to velocity-weakening friction and high fluid pressure and the critical nucleation size, continues to be a key factor in controlling the fault response. Simple periodic, period doubling and aperiodic aseismic oscillations appear as W/h^* increases. Both the maximum slip velocity V_{\max} and the recurrence period T_{cyc} of modeled transients increase with W/h^* , with the more significant fluctuations at larger W/h^* . The variation of V_{\max} with W/h^* , for fixed a/b , E and U , can be explained at least qualitatively using an analytical estimate that balances the mechanical energy release rate of a crack of width W with the fracture energy dominated by pore suction following an instantaneous velocity jump at the nucleation front. Comparing the slip velocity evolution processes during model transients with and without dilatancy at the same W/h^* , we found that the nucleation of transient slip under time-variant pore pressure appears well within the velocity-weakening zone. In both situations, the slip propagation speed v_r and the maximum velocity at the front V_{\max} satisfy the relation $v_r/V_{\max} = \gamma\mu'/\Delta\tau^{p-r}$, with a constant prefactor $\gamma \approx 0.6$, when the slip pulses are quasi-steady, although v_r and V_{\max} are much smaller than their counterparts without dilatancy. The pore pressure evolution (and $\Delta\tau^{p-r}$) can be approximated by an analytical solution of $\Delta p(t)$ following an instantaneous velocity jump from an initial state θ_i to a constant V_{\max} as the slip pulse propagates.

[43] Two important parameters are (1) $U = t_p/(d_c/V_{ss})$, the ratio between the characteristic diffusion time scale for pore pressure p on the sliding interface to equilibrate with its ambient level and the state variable evolution time scale at steady state velocity, and (2) $E = f_0(\epsilon/\beta)/(b\bar{\sigma}_0)$ which measures the relative contributions to the peak-to-residual stress drop from pore suction and from friction evolution. We showed that parameters U and E have similar effects on V_{\max} and T_{cyc} . As U or E increases toward 1, V_{\max} decreases as higher pore suction is induced, while T_{cyc} remains relatively constant due to the compensating effects of smaller velocity and longer sliding duration. For U (or E) greater than 1, V_{\max} in the velocity-weakening zone approaches the steady state rate at $\xi = W$, and an increasing T_{cyc} with U (or E) can be explained by the neutral stability period T_{ns} that is derived for a single-degree-of-freedom spring-slider sys-

tem with dilatancy. By adjusting the value of W/h^* according to the variation of the critical stiffness under dilatancy with U and E , we showed that the increasing trend of T_{cyc}/T_{ns} with W/h^* for over 3 orders of magnitude of U (or E) agrees very well with that defined in the absence of dilatancy.

[44] Using a Cascadia-like 2-D subduction fault model with the rate and state frictional properties measured for gabbro gouge, we showed that episodic aseismic transients can also exist for a much broader range of W/h^* due to dilatancy stabilization. For the relatively small values $U = 0.23$ and $E \lesssim 1.5$ used in the simulation cases, the adjustment in W/h^* is negligible, and the cumulative slip per episode and the recurrence period of modeled transients are comparable to those at the same W/h^* without dilatancy. They further follow the approximately linear trends of increasing slip and period beyond the aseismic-seismic boundary. By contrast, the maximum slip velocity during transients can be several orders of magnitude smaller than those at the same W/h^* without dilatancy. That difference becomes more significant at larger W/h^* .

Appendix A: Pore Pressure and Stress Drop Following a Velocity Step (“Aging” Law)

A1. Exact Solutions Under Special Conditions

[45] Following an instantaneous velocity jump from an initial state θ_i to a constant speed V_2 , the state variable evolution for sliding at V_2 as described by the “aging” law is

$$\frac{d\theta}{dt} = 1 - \frac{V_2\theta}{d_c}, \quad (\text{A1})$$

which can be integrated to

$$\theta(t) = \frac{d_c}{V_2} \left[1 - \left(1 - \frac{V_2\theta_i}{d_c} \right) e^{-V_2 t/d_c} \right]. \quad (\text{A2})$$

Substituting $\theta(t)$ into the rate and state friction equation (1), we get

$$f = f_0 + (a - b) \ln(V_2/V_0) + b \ln \left[1 - \left(1 - \frac{V_2\theta_i}{d_c} \right) e^{-\delta/d_c} \right], \quad (\text{A3})$$

where slip $\delta = V_2 t$. Defining the function

$$\mathcal{F} \left(\frac{\delta}{d_c}, \frac{V_2\theta_i}{d_c} \right) = \ln \left[1 - \left(1 - \frac{V_2\theta_i}{d_c} \right) e^{-\delta/d_c} \right], \quad (\text{A4})$$

and the residual friction

$$f^r = f_0 + (a - b) \ln(V_2/V_0), \quad (\text{A5})$$

we can write the friction as $f = f^r + b\mathcal{F}$. Let $\Delta p = p - p_0$ be the pore suction (relative to ambient), substituting equations (A1) and (A2) into (10) results in

$$\frac{d(\Delta p)}{dt} = -\frac{\Delta p}{t_p} + \frac{\epsilon}{\beta} \frac{V_2}{d_c} \left(\frac{e^{\delta/d_c}}{1 - V_2\theta_i/d_c} - 1 \right)^{-1}. \quad (\text{A6})$$

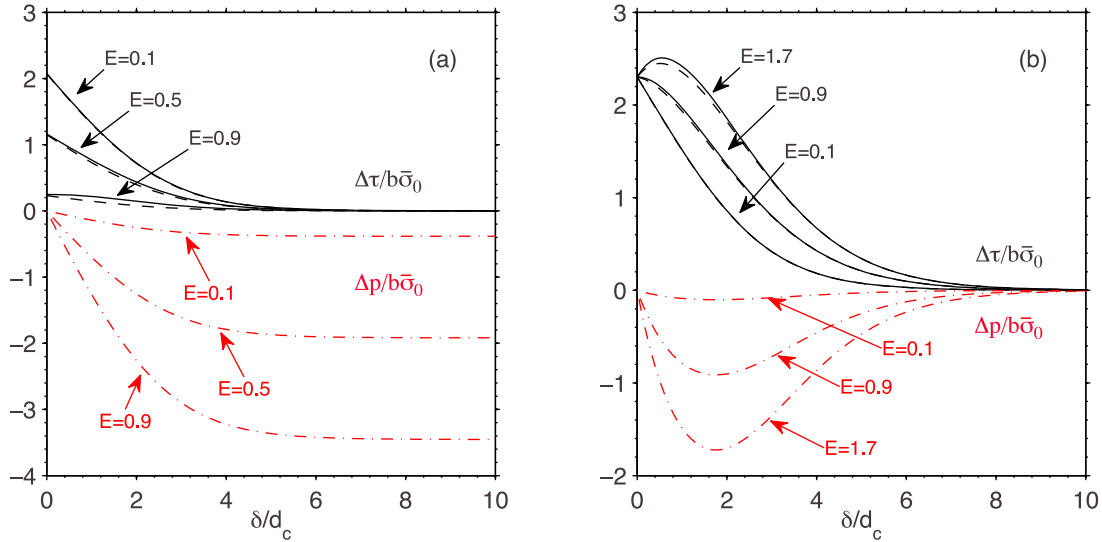


Figure A1. Evolution of shear stress drop $\Delta\tau = \tau - \tau^r$ (black solid line) and pore suction $\Delta p = p - p_0$ (red dash-dotted line), both normalized by $b\bar{\sigma}_0$, with slip δ/d_c . Parameters are $a/b = 0.9412$, $b = 0.034$, $f_0 = 0.6$, $V_2\theta_i/d_c = 10$. (a) Fully undrained scenario. Three cases for $E = 0.1, 0.5$, and 0.9 are shown here. Black dashed line shows the approximation in equation (A11). For small $E = 0.1$ and 0.5 , the difference is negligible. Even for a large $E = 0.9$, $(1 - E)\mathcal{F}$ still well represents the evolution of stress drop. Δp approaches $-(\epsilon/\beta)\ln(V_2\theta_i/d_c)$ as δ/d_c is sufficiently large. Fracture energy G_c (area beneath the stress drop curve) is smaller for larger E . (b) Partially drained scenario, where $U = V_2t_p/d_c = 1$. Three cases for $E = 0.1, 0.9$, and 1.7 are shown here. Black dashed line shows the approximation in equation (A15). G_c is greater for larger E . Pore pressure returns to the ambient level ($\Delta p = 0$) after sufficient slip.

Equation (A6) can be integrated analytically under the following special conditions.

[46] 1. Fault zone is fully undrained, which means t_p is infinitely long compared to the state evolution time scale. The $\Delta p/t_p$ term in (A6) becomes 0 and pore pressure evolves as

$$\begin{aligned} \Delta p(t) &= \frac{\epsilon}{\beta} \left[\ln \left(1 - \left(1 - \frac{V_2\theta_i}{d_c} \right) e^{-\delta/d_c} \right) - \ln \left(\frac{V_2\theta_i}{d_c} \right) \right] \\ &= \frac{\epsilon}{\beta} \left[\mathcal{F} - \ln \left(\frac{V_2\theta_i}{d_c} \right) \right]. \end{aligned} \quad (\text{A7})$$

The maximum pore suction is reached at $t \rightarrow \infty$:

$$\Delta p^r = \Delta p_{\max} = -(\epsilon/\beta) \ln(V_2\theta_i/d_c). \quad (\text{A8})$$

The shear stress drop in the evolution process is

$$\begin{aligned} \Delta\tau &= \tau - \tau^r = f(\bar{\sigma}_0 - \Delta p) - f^r(\bar{\sigma}_0 - \Delta p^r) \\ &= (f - f^r)\bar{\sigma}_0 - f\Delta p + f^r\Delta p^r \\ &= [b(\bar{\sigma}_0 - \Delta p^r) - (\epsilon/\beta)f^r]\mathcal{F} - b\frac{\epsilon}{\beta}\mathcal{F}^2 \end{aligned} \quad (\text{A9})$$

Substituting Δp^r and f^r to the above expression and normalizing $\Delta\tau$ by $b\bar{\sigma}_0$, we get

$$\frac{\Delta\tau}{b\bar{\sigma}_0} = \left[1 - E + \frac{bE}{f_0} \ln \left(\frac{V_2\theta_i}{d_c} \right) - \frac{E}{f_0} (a - b) \ln \left(\frac{V_2}{V_0} \right) \right] \mathcal{F} - \frac{bE}{f_0} \mathcal{F}^2, \quad (\text{A10})$$

where

$$E = \frac{f_0\epsilon/\beta}{b\bar{\sigma}_0}.$$

For a group of parameters $a/b = 0.9412$, $b = 0.034$, $f_0 = 0.6$, $V_2\theta_i/d_c = 10$ and assuming $V_0 = d_c/\theta_i$, the evolution of shear stress drop and pore suction, both normalized by $b\bar{\sigma}_0$, are shown in Figure A1a. For each chosen E , as slip becomes sufficiently large, pore pressure Δp approaches a constant value of $-(\epsilon/\beta)\ln(V_2\theta_i/d_c)$, and τ approaches τ^r . A larger E predicts higher pore pressure suction, and smaller fracture energy (area beneath the $\Delta\tau$ curve). The black dashed lines show the first two terms in equation (A10). For small values of E (such as 0.1 and 0.5 shown in Figure A1a), we can approximate the stress drop as

$$\frac{\Delta\tau}{b\bar{\sigma}_0} \approx (1 - E)\mathcal{F}. \quad (\text{A11})$$

[47] 2. Time scales for pore pressure reequilibration and state evolution are the same, i.e., $t_p = d_c/V_2$. In this situation, integration of equation (A6) gives

$$\begin{aligned} \Delta p(t) &= \frac{\epsilon}{\beta} \left(1 - \frac{V_2\theta_i}{d_c} \right) \\ &\cdot \left[\ln \left(1 - \frac{d_c}{V_2\theta_i} \right) + \ln \left(1 - \left(1 - \frac{V_2\theta_i}{d_c} \right)^{-1} e^{\delta/d_c} \right) \right] e^{-\delta/d_c}. \end{aligned} \quad (\text{A12})$$

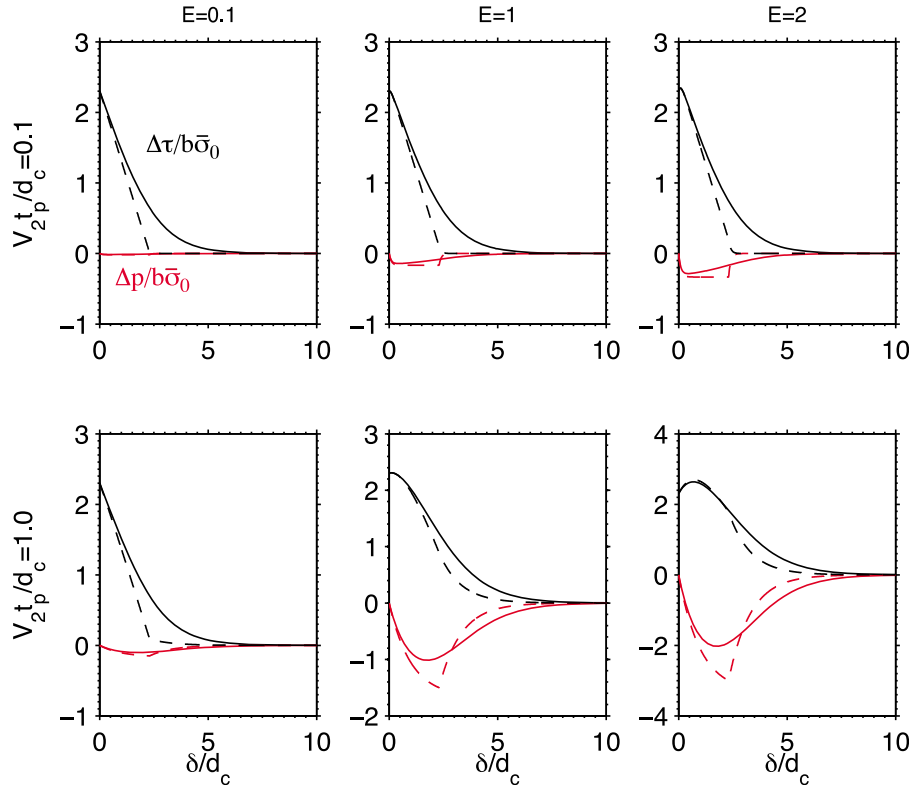


Figure A2. Evolution of shear stress drop $\Delta\tau$ (black) and pore suction Δp (red), normalized by $b\bar{\sigma}_0$, for various combinations of E and $U = V_2 t_p / d_c$, with parameters $a/b = 0.9412$, $b = 0.034$, $f_0 = 0.6$, and $V_2 \theta_i / d_c = 10$. Solid lines represent numerical solutions of equation (A6). Dashed lines are analytical solutions from equations (A23) to (A26). $U = V_2 t_p / d_c = 0.1$ and 1.0 (equivalently, $V_1 t_p / d_c = 0.01$ and 0.1) are used for cases in the first and second rows, respectively. $E = 0.1, 1.0$, and 2.0 are used for each column, from left to right. The analytical solutions generally agree well with the numerical solutions, with moderate overpredictions in $\Delta p(t)$ and the maximum pore suction.

As δ approaches ∞ , $\Delta p^r = 0$, such that the shear stress drop becomes

$$\begin{aligned} \Delta\tau &= (f - f^r)\bar{\sigma}_0 - f\Delta p \\ &= b\bar{\sigma}_0\mathcal{F} - \left[f_0 - b\left(1 - \frac{a}{b}\right) \ln\left(\frac{V_2}{V_0}\right) + b\mathcal{F} \right] \Delta p. \end{aligned} \quad (\text{A13})$$

Normalizing $\Delta\tau$ by $b\bar{\sigma}_0$, we get

$$\frac{\Delta\tau}{b\bar{\sigma}_0} = \mathcal{F} - E \left[1 - \frac{b(1 - a/b) \ln(V_2/V_0) - b\mathcal{F}}{f_0} \right] \frac{\Delta p}{\epsilon/\beta}. \quad (\text{A14})$$

Again, using parameters $a/b = 0.9412$, $b = 0.034$, $f_0 = 0.6$, $V_2 \theta_i / d_c = 10$ and assuming $V_0 = d_c / \theta_i$, the evolution of shear stress drop and pore suction, both normalized by $b\bar{\sigma}_0$, are shown in Figure A1b. Three cases for $E = 0.1, 0.9$ and 1.7 are calculated. Pore suction is larger for higher E values. The black dashed lines show stress drop approximated by the first two terms in equation (A14):

$$\frac{\Delta\tau}{b\bar{\sigma}_0} \approx \mathcal{F} - E \frac{\Delta p}{\epsilon/\beta}, \quad (\text{A15})$$

which agree very well with the exact stress drop.

[48] As $\Delta p < 0$, the second term becomes a positive contribution to $\Delta\tau$. We expect, for other partially drained conditions (with different $V_2 t_p / d_c$ ratios), fracture energy also increases with E as in this case. In the above two scenarios, the choice of a/b has a minor effect on the normalized stress drop since it does not appear in the leading terms in equations (A10) and (A14).

A2. Simplified Situation and General Analytical Solutions

[49] Immediately following a velocity step from an initial state θ_i to a constant speed V_2 , the state evolution is dominated by the term $-V_2 \theta / d_c$, provided $V_2 \theta / d_c \gg 1$. θ remains constant after reaching steady state. Under this assumption, equation (A1) can be simplified to

$$\frac{d\theta}{dt} = \begin{cases} -V_2 \theta / d_c & (t \leq t_0) \\ 0 & (t > t_0) \end{cases} \quad (\text{A16})$$

Thus, when $t \leq t_0$, $\theta(t) = \theta_i e^{-V_2 t / d_c}$, and when $t > t_0$, θ is a constant d_c / V_2 .

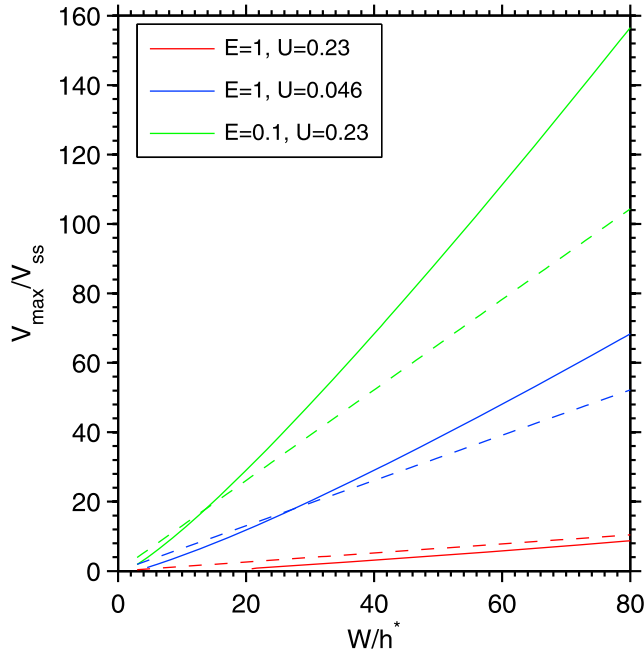


Figure B1. Analytical estimate of SSE maximum velocity V_{\max}/V_{ss} as functions of W/h^* , E , and U , based on the balance between pore suction dominated fracture energy and mechanical energy release rate for a crack governed by rate and state friction at partially drained condition. Red, blue, and green solid lines are plotted using equation (B2), with $E = 1$, $U = 0.23$, $E = 1$, $U = 0.046$, and $E = 0.1$, $U = 0.23$, respectively. Friction parameter $a/b = 0.9412$ for all three cases. Solid lines in Figure 2 show the same property but on a logarithm scale. Dashed lines show the linear dependence on W/h^* : $V_{\max}/V_{ss} = [(1 - a/b)/(2EU)](W/h^*)$ for comparison. For the range of W/h^* shown here, equation (B2) predicts V_{\max} increases only slightly faster than linearly with W/h^* .

[50] Substituting $\theta(t)$ into the rate and state friction equation (1), we get

$$f = f_0 + a \ln(V_2/V_0) + b \ln(V_0\theta_i/d_c) - b(V_2t/d_c), \quad (t \leq t_0) \quad (\text{A17})$$

with the residual friction coefficient $f^r = f_0 + a \ln(V_2/V_0) + b \ln(V_0\theta_i/d_c) - b(V_2t_0/d_c)$. The transition time t_0 is determined by equating f^r to the steady state friction $f_0 + (a - b) \ln(V_2/V_0)$:

$$t_0 = (d_c/V_2) \ln(V_2\theta_i/d_c). \quad (\text{A18})$$

The pore pressure evolution equation (10) becomes

$$\frac{d(\Delta p)}{dt} = \begin{cases} -\Delta p/t_p - \epsilon V_2/(\beta d_c) & (t \leq t_0) \\ -\Delta p/t_p & (t > t_0) \end{cases} \quad (\text{A19})$$

which integrates to

$$\Delta p(t) = \begin{cases} (\epsilon/\beta)(V_2t_p/d_c)[e^{-t/t_p} - 1] & (t \leq t_0) \\ \Delta p(t_0)e^{-(t-t_0)/t_p} & (t > t_0) \end{cases} \quad (\text{A20})$$

For $t \leq t_0$, the stress drop is

$$\begin{aligned} \Delta \tau &= (f - f^r)\bar{\sigma}_0 - f\Delta p \\ &= -b\bar{\sigma}_0 \frac{V_2}{d_c}(t - t_0) - \frac{\epsilon}{\beta} \frac{V_2t_p}{d_c} (e^{-t/t_p} - 1) \\ &\quad \cdot \left[f_0 + a \ln(V_2/V_0) + b \ln\left(\frac{V_0\theta_i}{d_c}\right) - b \frac{V_2t}{d_c} \right], \end{aligned} \quad (\text{A21})$$

and for $t > t_0$,

$$\begin{aligned} \Delta \tau &= -f^r \Delta p = -\Delta p(t_0) [e^{-(t-t_0)/t_p}] \\ &\quad \cdot \left[f_0 + a \ln(V_2/V_0) + b \ln\left(\frac{V_0\theta_i}{d_c}\right) - b \frac{V_2t_0}{d_c} \right]. \end{aligned} \quad (\text{A22})$$

With the definitions $\hat{t} = V_2t/d_c = \delta/d_c$, $\hat{t}_0 = V_2t_0/d_c = \delta_0/d_c = \ln(V_2\theta_i/d_c)$, $U = V_2t_p/d_c$ and $E = f_0 = (\epsilon/\beta)/(b\bar{\sigma}_0)$, the above equations of pore suction and shear stress drop can be rewritten as (for $\hat{t} \leq \hat{t}_0$)

$$\frac{\Delta p}{b\bar{\sigma}_0} = \frac{EU}{f_0} (e^{-\hat{t}/U} - 1), \quad (\text{A23})$$

$$\frac{\Delta \tau}{b\bar{\sigma}_0} = (\hat{t}_0 - \hat{t}) - b \left(\frac{\Delta p}{b\bar{\sigma}_0} \right) \left[\frac{f_0}{b} + \left(\frac{a}{b} - 1 \right) \ln(V_2/V_0) + \hat{t}_0 - \hat{t} \right], \quad (\text{A24})$$

and (for $\hat{t} > \hat{t}_0$)

$$\frac{\Delta p}{b\bar{\sigma}_0} = \frac{\Delta p(\hat{t}_0)}{b\bar{\sigma}_0} e^{-(\hat{t}-\hat{t}_0)/U}, \quad (\text{A25})$$

$$\frac{\Delta \tau}{b\bar{\sigma}_0} = -b \left(\frac{\Delta p}{b\bar{\sigma}_0} \right) \left[\frac{f_0}{b} + \left(\frac{a}{b} - 1 \right) \ln(V_2/V_0) \right], \quad (\text{A26})$$

where $\Delta p(\hat{t}_0) = (EU/f_0)(e^{-\hat{t}_0/U} - 1)$.

[51] Using parameters $a/b = 0.9412$, $b = 0.034$, $f_0 = 0.6$, $V_2\theta_i/d_c = 10$ and assuming $V_0 = d_c/\theta_i$, the evolution of shear stress drop and pore suction, normalized by $b\bar{\sigma}_0$, are shown in Figure A2. $\Delta \tau(t)$ and $\Delta p(t)$ from equations (A23) to (A26) generally agree well with those calculated by numerically solving equation (A6). For a constant U , the maximum pore suction increases proportionally with E , as evident in equations (A23) and (A25). The analytical solutions of $\Delta p(t)$ are moderately larger than the numerical solutions, which is responsible for the overpredictions in Figure 4d.

Appendix B: Analytical Estimate for Maximum Slip Rate

[52] As shown in Appendix A (equations (A23) to (A26) and Figure A2), following an instantaneous velocity jump from an initial state θ_i to a constant velocity V_2 , for $E = f_0(\epsilon/\beta)/(b\bar{\sigma}_0) \gtrsim 1$ and $U = V_2t_p/d_c \gtrsim 1$ the total fracture energy $G^c = \int_0^\infty \Delta \tau d\delta$ (area under the stress drop-slip curve) is dominated by the energy from pore suction

$$G_{\Delta p}^c = - \int_0^\infty f_0 \Delta p(\delta) d\delta = f_0 \left(\frac{\epsilon}{\beta} \right) V_2 t_p \ln \left(\frac{V_2 \theta_i}{d_c} \right), \quad (\text{B1})$$

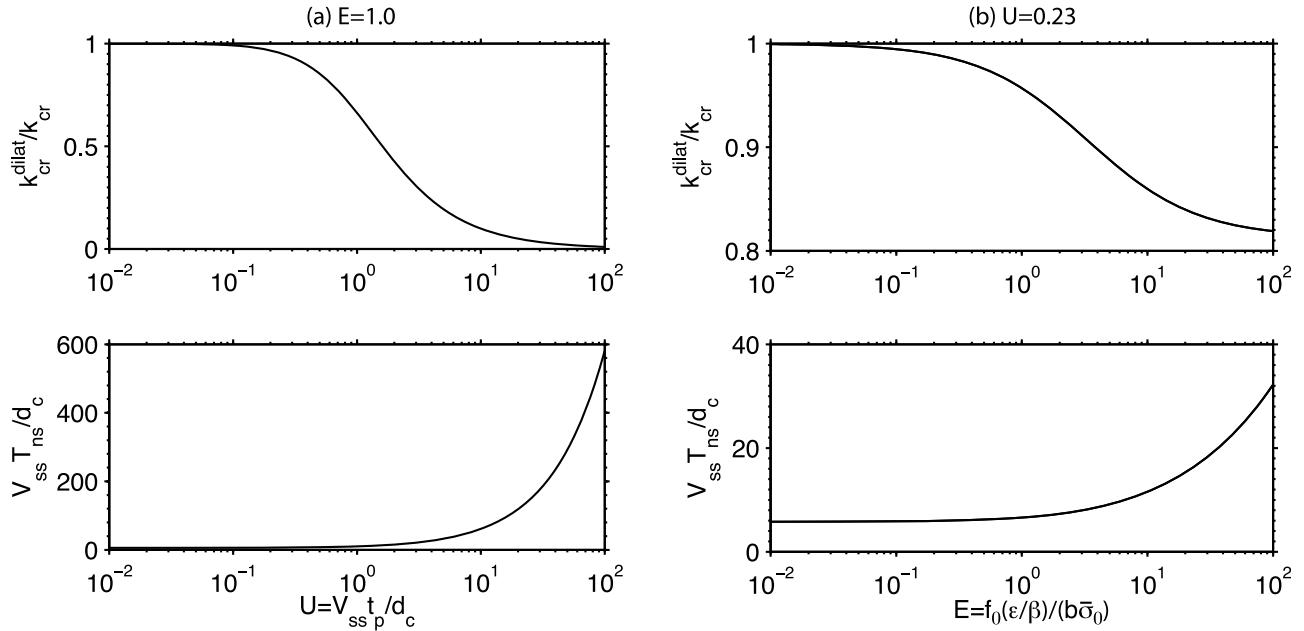


Figure C1. Dependence of nondimensional critical stiffness $\hat{K}_{cr} = k_{cr}^{dilat}/k_{cr}$ and neutral stability period $\hat{T}_{ns} = V_{ss} T_{ns}/d_c$ on (a) the drainage parameter U and (b) the dilatancy parameter E from linearized stability analysis, equations (C1) and (C5). $E = 1.0$ and $U = 0.23$ are constant in Figures C1a and C1b, respectively. Friction parameter $a/b = 0.9412$.

where $\Delta p(\delta)$ is defined in equations (A23) and (A25). This expression for $G_{\Delta p}^c$ is identical to that derived by *Segall et al.* [2010] for the “slip” law. Equating $G_{\Delta p}^c$ to the mechanical energy release rate $G = \pi W \Delta \tau^2 / (4\mu')$ for a crack of width W , where $\Delta \tau = (b - a)\bar{\sigma}_0 \ln(V_2/V_1)$ for any partially drained condition, and making the approximation that $\ln(V_2/V_1) \approx \ln(V_{max}/V_{ss})$, we get the following estimate of the maximum slip rate

$$\begin{aligned} \frac{V_{max}}{V_{ss}} \left[\ln \left(\frac{V_{max}}{V_{ss}} \right) \right]^{-1} &= \frac{1}{2} \frac{W}{h^*} \left(1 - \frac{a}{b} \right) \frac{d_c}{V_{ss} t_p} \frac{b \bar{\sigma}_0}{f_0 \epsilon / \beta} \\ &= \frac{1}{2EU} \left(1 - \frac{a}{b} \right) \frac{W}{h^*}. \end{aligned} \quad (\text{B2})$$

Note from the structure of equation (B2) that $V_{max} > V_{ss}$ will always be satisfied because the right hand side is always positive at velocity-weakening condition ($a/b < 1$). In addition, the equation has no solution when the right hand side term is less than constant e . This constraint puts a minimum limit for W/h^* when E and U are given. For $E = 1$ and $U = 0.23$, as shown in Figure 2, the red curve starts from $W/h^* \approx 21.6$ and $\log_{10}(V_{max}/V_{pl}) \approx -0.2$ (equivalent to $\ln(V_{max}/V_{ss}) = 1$ for $V_{ss}/V_{pl} = 0.23$).

[53] Equation (B2) predicts that for SSEs under such dilatancy conditions E and U that the peak-to-residual stress drop is dominated by pore suction, their maximum speed reached during the slipping process increases only slightly faster than linearly with W/h^* , as shown in Figure B1.

[54] In their linearized stability analysis of a spring-slider system with the “membrane diffusion” approximation, *Segall et al.* [2010] showed that under the condition of $E \gg$

$1 - a/b$ and $U \gg 1$ the critical crack width (before reaching instability) equals Uh^* ; here h^* is the drained characteristic nucleation size, as in equation (18). Associating the maximum velocity V_{max} with V^∞ (a velocity scale used by *Segall et al.* [2010] definition of the drainage parameter $U = V^\infty t_p/d_c$), they estimated

$$\frac{V_{max}}{V_{ss}} = \frac{W}{h^*} U^{-1}, \quad (\text{B3})$$

which predicts that V_{max} increases linearly with W/h^* and is independent of E and a/b .

Appendix C: Critical Stiffness and Neutral Stability Recurrence Period Under Dilatancy

[55] *Segall and Rice* [1995] and *Segall et al.* [2010] conducted a linearized stability analysis for a spring-slider system governed by rate and state friction with the membrane diffusion approximation. For the “slip” evolution law, they derived the critical stiffness k_{cr}^{dilat} (as in the no-dilatancy case, small perturbations from steady state grows to instability for spring stiffness k less than k_{cr}) and the oscillation period at neutral stability T_{ns} as a function of the dilatancy and drainage parameters E , U and of the friction parameter a/b . Their results are also valid for the “aging” law because in the vicinity of steady state these two evolution laws are asymptotically identical. The nondimensional form of the critical stiffness is

$$\hat{K}_{cr} = \frac{k_{cr}^{dilat} d_c}{\bar{\sigma}(b-a)} = \frac{k_{cr}^{dilat}}{k_{cr}} = 1 - E \left(\frac{1}{1 - a/b} \right) F(E, U, a/b), \quad (\text{C1})$$

where the function $F(E, U, a/b)$ is

$$F = \left[\frac{1 + \lambda + \omega}{2} - \sqrt{\frac{(1 + \lambda + \omega)^2}{4} - \omega} \right] \quad (C2)$$

$$\lambda = \frac{1}{E(U + U^2)} \frac{a}{b} \quad (C3)$$

$$\omega = \frac{U}{E(1 + U)} \left(1 - \frac{a}{b} \right). \quad (C4)$$

And the nondimensional neutral stability oscillation period is

$$\hat{T}_{ns} = \frac{T_{ns} V_{ss}}{d_c} = 2\pi U \sqrt{\frac{1}{F} - 1} \left(\frac{V_{ss}}{V_\infty} \right). \quad (C5)$$

For friction parameter $a/b = 0.9412$ as used in the simplified model in section 3.1, Figures C1a and C1b show the variation of \hat{K}_{cr} and \hat{T}_{ns} with the drainage parameter U and the dilatancy parameter E , with $E = 1.0$ and $U = 0.23$ fixed, respectively. It is clear that as the fault drainage degree increases (larger U), the critical stiffness decreases significantly, thus making the instability condition $k < k_{cr}^{dilat}$ less likely to be satisfied for a given spring stiffness k . As in Figure C1a, \hat{K}_{cr} quickly drops from 1 to nearly 0 as U increases from 0.1 to 100. Thus, for a given set of parameters E and a/b , the equivalent $W/h^*_{dilat} = Wk_{cr}^{dilat}/(\alpha\mu')$ decreases as U becomes larger than ~ 0.1 . This relation is used in the correction of W/h^* , as in equation (22), for all simulation cases with dilatancy. In contrast to the rapid decrease of \hat{K}_{cr} for $U > 0.1$, the variation of \hat{K}_{cr} with the dilatancy parameter E is relatively small; as shown in Figure C1b, for $U = 0.23$ and $a/b = 0.9412$, $\hat{K}_{cr} \approx 0.83$ at $E = 50$. As a result, the correction in W/h^* is small too.

[56] **Acknowledgments.** We thank Paul Segall and Jim Rice for thoughtful discussions along the preparation of this manuscript. Review comments by Jean-Paul Ampuero, Jon Samuelson, Kelin Wang, and an anonymous reviewer helped to clarify some concepts and to improve the presentation. This study was supported by a Department of Geosciences Hess postdoctoral fellowship to Yajing Liu at Princeton, USGS-NEHRP award 08HQGR0047 to Allan Rubin that partly supported Y. Liu, and the J. Lamar Worzel Assistant Scientist Fund to Y. Liu at WHOI.

References

- Ampuero, J.-P., and A. M. Rubin (2008), Earthquake nucleation on rate and state faults: c aging and slip laws, *J. Geophys. Res.*, *113*, B01302, doi:10.1029/2007JB005082.
- Audet, P., M. G. Bostock, N. I. Christensen, and S. M. Peacock (2009), Seismic evidence for overpressured subducted oceanic crust and megathrust fault sealing, *Nature*, *457*, 76–78, doi:10.1038/nature07650.
- Beeler, N. M., T. E. Tullis, and J. D. Weeks (1994), The roles of time and displacement in the evolution effect in rock friction, *Geophys. Res. Lett.*, *21*(18), 1987–1990, doi:10.1029/94GL01599.
- Blanpied, M. L., C. J. Marone, D. A. Lockner, J. D. Byerlee, and D. P. King (1998), Quantitative measure of the variation in fault rheology due to fluid-rock interactions, *J. Geophys. Res.*, *103*(B5), 9691–9712, doi:10.1029/98JB00162.
- Christensen, N. I. (1984), Pore pressure and oceanic crustal seismic structure, *Geophys. J. R. Astron. Soc.*, *79*, 411–423.
- Clarke, G. K. C. (1987), Subglacial till: A physical framework for its properties and processes, *J. Geophys. Res.*, *92*(B9), 9023–9036, doi:10.1029/JB092iB09p09023.

- Cochard, A., and J. R. Rice (1997), A spectral method for numerical elastodynamic fracture analysis without spatial replication of the rupture event, *J. Mech. Phys. Solids*, *45*, 1393–1418, doi:10.1016/S0022-5096(97)00004-5.
- Dieterich, J. H. (1979), Modeling of rock friction: 1. Experimental results and constitutive equations, *J. Geophys. Res.*, *84*(B5), 2161–2168, doi:10.1029/JB084iB05p02161.
- Dragert, H., R. D. Hyndman, G. C. Rogers, and K. Wang (1994), Current deformation and the width of the seismogenic zone of the northern Cascadia subduction thrust, *J. Geophys. Res.*, *99*(B1), 653–668, doi:10.1029/93JB02516.
- Dragert, H., K. Wang, and T. S. James (2001), A silent slip event on the deeper Cascadia subduction interface, *Science*, *292*(5521), 1525–1528, doi:10.1126/science.1060152.
- Gomberg, J., J. L. Rubinstein, Z. Peng, K. C. Creager, J. Vidale, and P. Bodin (2008), Widespread triggering of nonvolcanic tremor in California, *Science*, *319*(5860), 173, doi:10.1126/science.1149164.
- Hacker, B. R., G. A. Abers, and S. M. Peacock (2003), Subduction factory: 1. theoretical mineralogy, densities, seismic wave speeds, and H₂O contents, *J. Geophys. Res.*, *108*(B1), 2029, doi:10.1029/2001JB001127.
- He, C., Z. Wang, and W. Yao (2007), Frictional sliding of gabbro gouge under hydrothermal conditions, *Tectonophysics*, *445*, 353–362, doi:10.1016/j.tecto.2007.09.008.
- Hillers, G., and S. A. Miller (2007), Dilatancy controlled spatiotemporal slip evolution of a sealed fault with spatial variations of the pore pressure, *Geophys. J. Int.*, *168*, 431–445, doi:10.1111/j.1365-246X.2006.03167.x.
- Hirose, H., K. Hirahara, F. Kimata, N. Fujii, and S. Miyazaki (1999), A slow thrust slip event following the two 1996 Hyuganada earthquakes beneath the Bungo Channel, southwest Japan, *Geophys. Res. Lett.*, *26*(21), 3237–3240, doi:10.1029/1999GL010999.
- Hyndman, R. D., and K. Wang (1995), The rupture zone of Cascadia great earthquakes from current deformation and the thermal regime, *J. Geophys. Res.*, *100*(B11), 22,133–22,154, doi:10.1029/95JB01970.
- Ida, Y. (1973), The maximum acceleration of seismic ground motion, *Bull. Seismol. Soc. Am.*, *63*, 959–968.
- Ide, S., D. R. Shelly, and G. C. Beroza (2007), Mechanism of deep low-frequency earthquakes: Further evidence that deep nonvolcanic tremor is generated by shear slip on the plate interface, *Geophys. Res. Lett.*, *34*, L03308, doi:10.1029/2006GL028890.
- Iverson, N. R., T. S. Hooyer, and R. W. Baker (1998), Ring-shear studies of till deformation: Coulomb-plastic behavior and distributed strain in glacier beds, *J. Glaciol.*, *44*, 634–642.
- Iverson, R. M., M. E. Reid, N. R. Iverson, R. G. LaHusen, M. Logan, J. E. Mann, and D. L. Brien (2000), Acute sensitivity of landslide rates to initial soil porosity, *Science*, *290*, 513–516, doi:10.1126/science.290.5491.513.
- Kodaira, S., T. Iidaka, A. Kato, J. O. Park, T. Iwasaki, and Y. Kaneda (2004), High pore fluid pressure may cause silent slip in the Nankai trough, *Science*, *304*(5675), 1295–1298, doi:10.1126/science.1096535.
- Lachenbruch, A. H. (1980), Frictional heating, fluid pressure, and the resistance to fault motion, *J. Geophys. Res.*, *85*(B11), 6097–6112, doi:10.1029/JB085iB11p06097.
- Lapusta, N., and J. R. Rice (2003), Nucleation and early seismic propagation of small and large events in a crustal earthquake model, *J. Geophys. Res.*, *108*(B4), 2205, doi:10.1029/2001JB000793.
- Lapusta, N., J. R. Rice, Y. Ben-Zion, and G. Zheng (2000), Elastodynamic analysis for slow tectonic loading with spontaneous rupture episodes on faults with rate- and state-dependent friction, *J. Geophys. Res.*, *105*(B10), 23,765–23,789, doi:10.1029/2000JB900250.
- Liu, Y., and J. R. Rice (2005a), Aseismic slip transients emerge spontaneously in three-dimensional rate and state modeling of subduction earthquake sequences, *J. Geophys. Res.*, *110*, B08307, doi:10.1029/2004JB003424.
- Liu, Y., and J. R. Rice (2005b), Pore pressure evolution in shallow subduction earthquake sequences and effects on aseismic slip transients—Numerical modeling with rate and state friction, *Eos Trans. AGU*, *86*(52), Fall Meet. Suppl., Abstract T11E-05.
- Liu, Y., and J. R. Rice (2007), Spontaneous and triggered aseismic deformation transients in a subduction fault model, *J. Geophys. Res.*, *112*, B09404, doi:10.1029/2007JB004930.
- Liu, Y., and J. R. Rice (2009), Slow slip predictions based on granite and gabbro friction data compared to GPS measurements in northern Cascadia, *J. Geophys. Res.*, *114*, B09407, doi:10.1029/2008JB006142.
- Liu, Y., and A. M. Rubin (2010), Effects of fault gouge dilatancy on subduction zone earthquakes, *Eos Trans. AGU*, *90*(52), Fall Meet. Suppl., Abstract T24A-07.
- Lockner, D. A., and J. D. Byerlee (1994), Dilatancy in hydraulically isolated faults and the suppression of instability, *Geophys. Res. Lett.*, *21*(22), 2353–2356, doi:10.1029/94GL02366.

- Lowry, A. R., K. M. Larson, V. Kostoglodov, and R. Bilham (2001), Transient fault slip in Guerrero, southern Mexico, *Geophys. Res. Lett.*, *28*(19), 3753–3756, doi:10.1029/2001GL013238.
- Marone, C., C. B. Raleigh, and C. H. Scholz (1990), Frictional behavior and constitutive modeling of simulated fault gouge, *J. Geophys. Res.*, *95*(B5), 7007–7025, doi:10.1029/JB095iB05p07007.
- Mase, C. W., and L. Smith (1987), Effects of frictional heating on the thermal, hydrologic, and mechanical response of a fault, *J. Geophys. Res.*, *92*(B7), 6249–6272, doi:10.1029/JB092iB07p06249.
- McCaffrey, R. (2009), Time-dependent inversion of three-component continuous GPS for steady and transient sources in northern Cascadia, *Geophys. Res. Lett.*, *36*, L07304, doi:10.1029/2008GL036784.
- Miyazawa, M., and J. Mori (2006), Evidence suggesting fluid flow beneath Japan due to periodic seismic triggering from the 2004 Sumatra-Andaman earthquake, *Geophys. Res. Lett.*, *33*, L05303, doi:10.1029/2005GL025087.
- Obara, K. (2002), Nonvolcanic deep tremor associated with subduction in southwest Japan, *Science*, *296*(5573), 1679–1681, doi:10.1126/science.1070378.
- Peacock, S. M., K. Wang, and A. M. McMahon (2002), Thermal structure and metamorphism of subducting oceanic crust: Insight into Cascadia intraslab earthquakes, in *The Cascadia Subduction Zone And Related Subduction Systems: Seismic Structure, Intraslab Earthquakes and Processes, and Earthquake Hazards*, edited by S. Kirby, K. Wang, and S. Dunlop, pp. 123–126, U.S. Geol. Surv., Denver, Colo.
- Peng, Z., J. Vidale, K. C. Creager, J. L. Rubinstein, J. Gomberg, and P. Bodin (2008b), Strong tremor near Parkfield, CA, excited by the 2002 Denali Fault earthquake, *Geophys. Res. Lett.*, *35*, L23305, doi:10.1029/2008GL036080.
- Rice, J. R. (1993), Spatiotemporal complexity of slip on a fault, *J. Geophys. Res.*, *98*(B6), 9885–9907, doi:10.1029/93JB00191.
- Rice, J. R., N. Lapusta, and K. Ranjith (2001), Rate and state dependent friction and the stability of sliding between elastically deformable solids, *J. Mech. Phys. Solids*, *49*, 1865–1898, doi:10.1016/S0022-5096(01)00042-4.
- Rubin, A. M. (2008), Episodic slow slip events and rate-and-state friction, *J. Geophys. Res.*, *113*, B11414, doi:10.1029/2008JB005642.
- Rubin, A. M., and J.-P. Ampuero (2005), Earthquake nucleation on (age) rate and state faults, *J. Geophys. Res.*, *110*, B11312, doi:10.1029/2005JB003686.
- Rubinstein, J. L., J. Vidale, J. Gomberg, P. Bodin, K. C. Creager, and S. Malone (2007), Nonvolcanic tremor driven by large transient shear stresses, *Nature*, *448*, 579–582, doi:10.1038/nature06017.
- Rudnicki, J. W., and C.-H. Chen (1988), Stabilization of rapid frictional slip on a weakening fault by dilatant hardening, *J. Geophys. Res.*, *93*(B5), 4745–4757, doi:10.1029/JB093iB05p04745.
- Ruina, A. L. (1983), Slip instability and state variable friction laws, *J. Geophys. Res.*, *88*(B12), 10,359–10,370, doi:10.1029/JB088iB12p10359.
- Samuelson, J., D. Elsworth, and C. Marone (2009), Shear-induced dilatancy of fluid saturated faults: Experiment and theory, *J. Geophys. Res.*, *114*, B12404, doi:10.1029/2008JB006273.
- Schmitt, S. V., and P. Segall (2008), Shear heating-induced thermal pressurization during the nucleation of earthquakes, *Eos Trans. AGU*, *89*(53), Fall Meet. Suppl., Abstract T21D-08.
- Schmitt, S. V., P. Segall, and T. Matsuzawa (2007), Thermal pressurization is significant during earthquake nucleation, before seismic slip, *Eos Trans. AGU*, *88*(52), Fall Meet. Suppl., Abstract S12B-02.
- Schofield, A. N., and C. P. Wroth (1968), *Critical State Soil Mechanics*, 310 pp., McGraw-Hill, New York.
- Segall, P., and J. R. Rice (1995), Dilatancy, compaction, and slip instability of a fluid-infiltrated fault, *J. Geophys. Res.*, *100*(B11), 22,155–22,171, doi:10.1029/95JB02403.
- Segall, P., and J. R. Rice (2006), Does shear heating of pore fluid contribute to earthquake nucleation? *J. Geophys. Res.*, *111*, B09316, doi:10.1029/2005JB004129.
- Segall, P., and A. Rubin (2007), Dilatancy stabilization of frictional sliding as a mechanism for slow slip events, *Eos Trans. AGU*, *88*(52), Fall Meet. Suppl., Abstract T13F-08.
- Segall, P., A. M. Rubin, A. M. Bradley, and J. R. Rice (2010), Dilatant strengthening as a mechanism for slow slip events, *J. Geophys. Res.*, doi:10.1029/2010JB007449, in press.
- Shelly, D. R., G. C. Beroza, S. Ide, and S. Nakamura (2006), Low-frequency earthquakes in Shikoku, Japan, and their relationship to episodic tremor and slip, *Nature*, *442*(7099), 188–191, doi:10.1038/nature04931.
- Shibazaki, B., and T. Shimamoto (2007), Modelling of short-interval silent slip events in deeper subduction interfaces considering the frictional properties at the unstable-stable transition regime, *Geophys. J. Int.*, *171*(1), 191–205, doi:10.1111/j.1365-246X.2007.03434.x.
- Sibson, R. H. (1973), Interactions between temperature and pore fluid pressure during earthquake faulting and a mechanism for partial or total stress relief, *Nature*, *243*(126), 66–68.
- Sleep, N. H. (1995), Ductile creep, compaction, and rate and state dependent friction within major fault zones, *J. Geophys. Res.*, *100*(B7), 13,065–13,080, doi:10.1029/94JB03340.
- Sleep, N. H., and M. L. Blanpied (1992), Creep, compaction and the weak rheology of major faults, *Nature*, *359*(6397), 687–692, doi:10.1038/359687a0.
- Taylor, M. A. J., and J. R. Rice (1998), Dilatant stabilization of subduction earthquake rupture into shallow thrust interface, *Eos Trans. AGU*, *79*(45), Fall Meet. Suppl., F631.
- Wada, I., K. Wang, J. He, and R. D. Hyndman (2008), Weakening of the subduction interface and its effects on surface heat flow, slab dehydration, and mantle wedge serpentinization, *J. Geophys. Res.*, *113*, B04402, doi:10.1029/2007JB005190.
- Wang, K., R. Wells, S. Mazzotti, R. D. Hyndman, and T. Sagiya (2003), A revised dislocation model of interseismic deformation of the Cascadia subduction thrust, *J. Geophys. Res.*, *108*(B1), 2026, doi:10.1029/2001JB001227.

Y. Liu, Department of Geology and Geophysics, Woods Hole Oceanographic Institution, Clark South 285, MS 24, Woods Hole, MA 02543, USA. (yliu@whoi.edu)

A. M. Rubin, Department of Geosciences, Princeton University, 319 Guyot Hall, Princeton, NJ 08544, USA. (arubin@princeton.edu)